crystals

MDPI

Article

Multimodal Spectroscopy Assays for Advanced Nano-Optics Approaches by Tuning Nano-Tool Surface Chemistry and Metal-Enhanced Fluorescence

Marcelo R. Romero [1], Alicia V. Veglia [2], Maria Valeria Amé [3] and Angel Guillermo Bracamonte [2,*]

[1] Departamento de Química Orgánica, Facultad de Ciencias Químicas, Universidad Nacional de Córdoba, IPQA−CONICET, Medina Allende y Haya de la Torre, Córdoba 5000, Argentina; marcelo.ricardo.romero@unc.edu.ar
[2] Instituto de Investigaciones en Físico Química de Córdoba (INFIQC), Departamento de Química Orgánica, Facultad de Ciencias Químicas, Universidad Nacional de Córdoba, Ciudad Universitaria, Córdoba 5000, Argentina; aveglia@unc.edu.ar
[3] Centro de Investigaciones en Bioquímica Clínica e Inmunología (CIBICI), Departamento de Bioquímica Clínica, Facultad de Ciencias Químicas, UNC, Ciudad Universitaria, Córdoba 5000, Argentina; valeria.ame@unc.edu.ar
* Correspondence: gbracamonte@unc.edu.ar or guillermobrac@yahoo.ca

Abstract: In this research work, different chemical modifications were applied to gold nanoparticles and their use in enhanced non-classical light emitters based on metal-enhanced fluorescence (MEF) was evaluated. In order to achieve this, gold core–shell nanoparticles with silica shells were modified via multilayered addition and the incorporation of a covalently linked laser dye to develop MEF. Their inter-nanoparticle interactions were evaluated by using additional silica shell multilayers and modified cyclodextrin macrocycles. In this manner, the sizes and chemical surface interactions on the multilayered nanoarchitectures were varied. These optical active nanoplatforms led to the development of different nanoassembly sizes and luminescence behaviors. Therefore, the interactions and nanoassembly properties were evaluated by using various spectroscopic and nanoimaging techniques. Highly dispersible gold core–shell nanoparticles with diameters of 50–60 nm showed improved colloidal dispersion that led to single ultraluminescent gold core–shell nanoparticles with MEF. Then, the addition of variable silica lengths produced increased interactions and consequent nanoaggregation. However, the silanized nanoparticles were easily dispersible after agitation or sonication. Thus, their sizes were proportional only to the diameter and the van de Waals interaction did not affect their sizes in bulk. Then, the covalent linking of different concentrations of modified cyclodextrins was applied to the chemical surfaces by incorporating additional hydroxyl groups from the glucose monomeric unities of cyclodextrins. In this manner, variable larger-sized and inter-branched grafted gold core–shell silica nanoparticles were generated. The ultraluminescent properties were conserved due to the non-optical activity of the cyclodextrins. However, they generated enhanced ultraluminescence phenomena. Laser fluorescence microscopy nanoimaging showed enhanced resolutions in comparison to non-grafted supramolecular gold core–shell nanoparticles. The differences in their interactions and the sizes of the nanoassemblies were explained by their single nanoparticle diameters and the interacting chemical groups on their nanosurfaces. While the varied luminescence emissions generated were tuned by plasmonics, enhanced plasmonic phenomena and light scattering properties were seen depending on the type of nanoassembly. Thus, optically active and non-optically active materials led to different optical properties in the bright field and enhanced the excited state within the electromagnetic near-field of the gold nanotemplates. In this manner, it was possible to achieve high sensitivity by varying the spacer lengths and optical properties. Therefore, further perspectives regarding the design of nano-tools composed of light for various applications were discussed.

Keywords: nanochemistry; multilayered architectures; metal-enhanced fluorescence (MEF); nano-tools; enhanced non-classical light; nanomolecular interactions; nano-interactions; nanoaggregation; nanosensing

Citation: Romero, M.R.; Veglia, A.V.; Amé, M.V.; Bracamonte, A.G. Multimodal Spectroscopy Assays for Advanced Nano-Optics Approaches by Tuning Nano-Tool Surface Chemistry and Metal-Enhanced Fluorescence. *Crystals* **2024**, *14*, 338. https://doi.org/10.3390/cryst14040338

Academic Editor: Ye Zhu

Received: 9 March 2024
Revised: 25 March 2024
Accepted: 28 March 2024
Published: 31 March 2024

1. Introduction

In the last few years, the design and synthesis of nanomaterials have been of high interest due to their impact in targeted nanotechnology, which is relevant to many disciplines and research fields [1]. In this regard, the development of nano-optics is highly desirable and is directly associated with technological development. In order to accomplish this, the study of the generation of non-classical light [2] based on the interaction of photons and various matter compositions is currently being undertaken [3]. In a similar manner, the generation of high-energy electromagnetic fields from different sources, such as carbon-based materials [4] and inorganic nanostructured particles and substrates [5], could generate interactions with their immediate surroundings, modifying the electronic properties of the joined matter. In this manner, the nanophotonics produced, for example, by confined laser dyes within the nanoscale could result in different photophysics and applications [6]. Moreover, confined matter could produce quantum emitters, generating the well-known quantum dots, with different technological applications in comparison to other matter compositions [7].

In this context, to tune non-classical light, it is necessary to control both the nanoscale and quantum scale. This challenge is dependent on the optical approach used. Thus, nanoformulations within colloidal dispersions, obtained by applying wet chemical methods such as noble metal nanoparticle synthesis, and inorganic and organic quantum dots are of high interest. Moreover, the chemical modification of nanoparticles with various polymeric and molecular agents is currently used for different bottom-up processes. Core–shell nanoparticles and their multilayered modification provide versatile nanoarchitectures that offer multiple functionalities depending on the specific needs [8]. Their development could lead to nanoelectronics, nanoemitters, smart responsive nanomaterials, nanosensors, and hybrid nanomaterials with biomaterials, culminating in nano-biotechnology [9,10].

In this bottom-up process, the generation of enhanced nano-optics and devices that can be remotely activated is of high interest. Thus, one can highlight the luminescence and ultraluminescence properties associated with signal transduction in nano-technological applications. They are of high interest due to their impact on multiple new nanomaterials and metamaterials for the development of nano-devices. In this context, the nano-emitters should operate at the small or ultrasmall nanoscale depending on the application. In order to increase the quantum yields of fluorophores and emission signals, metal-enhanced fluorescence (MEF) has been applied and developed. This effect is based on the plasmonic interaction of the electronic oscillation of a metallic surface with the fluorophores in the near-field [11,12]. This phenomenon produces enhancements ranging from 2 to 100, depending on the nanostructural parameters, experimental variables, and instrumental setups [13–15]. The principal parameters are the coupling of the plasmonic fluorophores in the basal state to increase the occupied excited state levels and, in this manner, to achieve faster radiative relaxation [16]. Due to this increase, based on the high intensity of the electromagnetic field generated by the metallic surface in the near-field, the distance from the metallic surface to the fluorophore is another important variable to be controlled in nanoparticle design [17,18].

However, their chemical surface modifications could affect the inter-nanoparticle interactions and nano-optical properties. In addition, the incorporation of other nanomaterials, macromolecules, and supra-molecular systems could lead to tunable functions depending on the matter considered. Therefore, the whole modified nanoarchitecture could affect or tune their properties. In this regard, ultraluminescent gold core–shell nanoparticles with ultraluminescent properties were recently synthesized based on MEF [19], and at the same time, supramolecular grafted gold nanoparticles modified with varied molecular spacers produced different nano-optical phenomena depending of their nano-assembling behavior [20]. In this regard, in the present research manuscript, we propose the design and synthesis of cyclodextrin grafted gold core–shell silica nanoparticles to tune nano-assembling and study nano-optic behaviors [1].

2. Materials and Methods

2.1. Reagents

Water was obtained using a Millipore apparatus. Rhodamine B (RhB; (99% purity, Sigma-Aldrich, USA), hydrogen tetrachloroaurate, $HAuCl_4.3H_2O$ (99%, Sigma-Aldrich, St. Louis, MO, USA), citrate sodium tribasic dehydrate (99%, ACS reagent), and polyvinyl pyrrolidone (PVP) 40,000 g/mol, (98%, Sigma-Aldrich, USA) were used.

Tetraethyl orthosilicate (TEOS) (98%, Sigma-Aldrich, USA), Ethanol (Sintorgan, HPLC grade, Buenos Aires, Argentine), 3-(aminopropyl)triethoxysilane (APS) (98%, Sigma-Aldrich, USA), N-hydroxi-succinimide (NHS), and N-(3-Dimethylaminopropyl)-N′-ethylcarbodiimide hydrochloride (EDC) (98%, Sigma-Aldrich, USA) were used, as well as sodium cyanide (95%, Sigma-Aldrich, USA).

βcyclodextrins (βCD) (98% purity, Sigma, Oakville, ON, Canada), tosyl chloride, and imidazole reactants were from Sigma-Aldrich, USA. The pH = 7.4 (10 mM) buffer was prepared according to literature procedures (2.3 mM monosodium dihydrogen phosphate and disodium hydrogen phosphate 7.7 mM). All buffer constituents were commercial analytical-grade reagents. DMF was an ACS reagent from Sintorgan Company, Villa Martelli, Buenos Aires, Argentine.

For in-flow cytometry, standard micro-meter multicolored fluorescent beads were purchased from BD Company, Franklin Lakes, NJ, USA.

2.2. Apparatus

UV–vis and spectrofluorimetric determinations were carried out in a Varian UV-50 Carry 50 Conc. and a Cary-Eclypse (USA), respectively. Lifetime measurements were carried out with a PicoQuant, Fluotime 2000 (Berlin, Germany).

Dynamic Light Scattering (DLS) measurements were carried out with Particle size-zeta potential particle analyzer Delsa™Nano Submicron from Malvern Company (Westborough, MA, USA).

OLYMPUS Confocal Laser Scanning, FV1200, FLUOVIEW (USA) was used for the fluorescence microscopy images.

Transmission electron microscopy (TEM) images were taken using a TEM JEM-1230, JEOL (Peabody, MA, USA) with an operating voltage of 200 kV.

An ultrasonic bath (Branson 2510) was used for the dispersion of the reagents and colloidal dispersions. The centrifugation was carried out using the Eppendorf Centrifuge 5804 (rpm range 7500–8000 rpm).

Infrared imaging and spectra were recorded with Nicolet iN10 MX Instrument. It contained an infrared imaging microscope with FT-IR optics.

The flow cytometer was purchased from BD Company. The model used was FACSCanto II analyzer (BD Biosciences, San Jose, CA, USA). The data were analyzed with FlowJo V10 software (TreesStar) and FacsDiva software 2022. Laser excitation at 488.0 nm and 555.0 nm with standard filters at 533/30 and 585/40 for Alexa Fluor 488-A and AF5555-A standard emission recording was applied. Laser excitations were also used at 561.0 nm with emission filters at 595/40 nm, for PE-A. The Alexa Fluor 488-A, AF5555-A, and PE-A were used as standard set-up parameters of the In-Flow Cytometry instrument. They were related to spectroscopical properties associated with well-known fluorescent dyes such as Alexa Fluor 488 (Alexa Fluor 488-A), Alexa-Fluor 555 AF5555-A, and R-phycoerythrin (PE-A), respectively. Data analysis was performed with Origin (Scientific Graph system) version 8.

2.3. General Procedure

The gold nanoparticles were synthesized by the citrate reduction method [21] of $HAuCl_4$ and were afterward covered with PVP 40. The resulting nanoparticles were then redispersed in anhydrous ethanol (mother solution, [Au NPs] = 3.97×10^{10} NPs/mL, diameter = 40.0 nm). After that, the surface of the nanoparticles was modified with variable silica spacer lengths obtained by the classical Storber method [22]. For a typical synthesis

of gold core–shell nanoparticles (d40 Au@SiO_2), 10 nm silica shell 7.0 µL of TEOS 10% (at pH = 8–9 by addition of NH_4OH) was added vigorously to 4 mL of PVP-covered gold nanoparticles. This procedure followed the previous method described by us with TEOS additions [23]. The covalent bonding of RhB with APS by NHS/EDC activation was to obtain Fl-APS conjugated solution. For Fl linking over the silica surface, increasingly variable volumes of this solution were added to 1 mL of d40 Au@SiO_2 with continuous stirring. The reaction time was 20 min, and immediately after a second, a thin silica shell was added via a solution of TEOS 2.5%. The reaction was allowed to proceed for 24 h to obtain the nanoarchitecture (d40 Au@SiO_2-RhB) (Scheme 1).

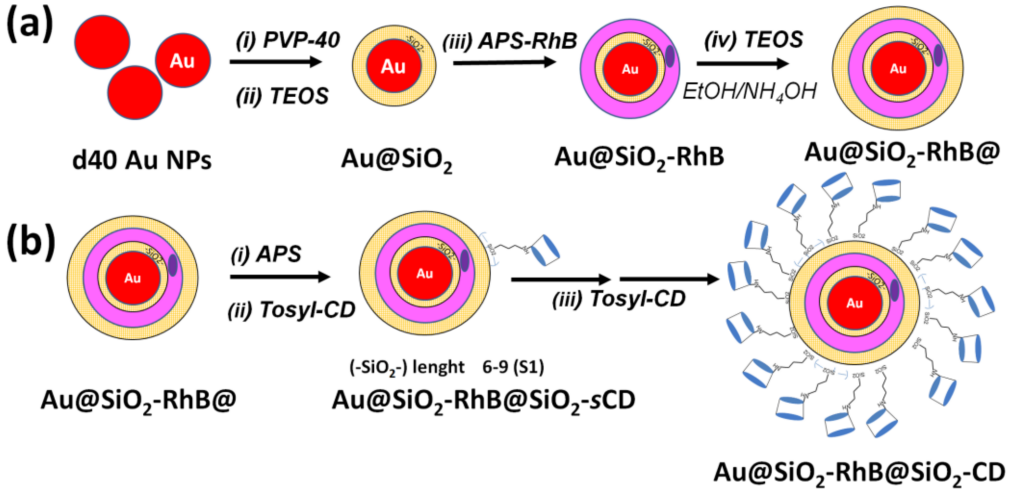

Scheme 1. Schema of synthesis steps of multi-layered cyclodextrin grafted gold core–shell nanoparticles (Au@SiO_2RhB-CD): (**a**) (i) PVP-stabilized nanoparticles with addition of PVP-40 and (ii) TEOS in basic media formed the gold core–shell nanoparticles (d40 Au@SiO_2); after (iii) and (iv), APS-RhB conjugated on silanized Au@SiO_2 was added, as well as nanoscale SiO_2 as protective layer by TEOS/Basic ethanolic media, with a few nanometers. (**b**) (i) Amine grafting of d40 Au@SiO_2 with APS addition, then (ii) supramolecular grafting by addition of Tosylated beta-cyclodextrin (Tosyl.CD), and (iii) to obtain per-grafted (Au@SiO_2RhB-pCD) varying additions and concentrations by steps, or single-grafted cyclodextrins (Au@SiO_2RhB-sCD) on core–shell nanoparticles by multi-ultra-diluted additions.

After the surfaces of these ultraluminescent gold core–shell nano-acceptors (Au@SiO_2-RhB) were modified with average constant silica spacer lengths of 9.5 nm obtained by the Störber method [24] (Scheme 1(bi)), aliquots of µL volume from TEOS 10% (at pH = 8–9 by addition of NH_4OH) were added vigorously to 4 mL sample (s1–s4) of gold core–shell silica nanoparticles (gold concentrated nanoparticles; [Au NPs] = 5.00 × 10^{10} NPs/mL) to obtain silanized ultraluminescent gold core–shell nano-emitter platforms for further supramolecular grafting (Au@SiO_2-RhB-).

Then, the silanized ultraluminescent gold core–shell nano-emitter (Au@SiO_2-RhB-) platform was modified with amine groups by the addition of APS (Scheme 1(bii)). For 5 mL of gold nanoparticles in ethanol, 50 µL of APS was added and allowed to react for 2 h at room temperature. Nanoparticles were centrifuged and washed with ethanol. To confirm the presence of amine sites over the surface, it was assayed with a specific reagent used in proteins, 2,4,6-Trinitrobenzenesulfonic acid solution (TNBS), measuring an absorbance band at 340 nm [25]. At this point, the amine-functionalized surface of the nanoparticles (Au@SiO_2-RhB-NH_2) was ready to react with activated tosyl-βCD (Scheme 1(biii)).

The tosylation of the βCD was carried out by a modified methodology from the literature for the synthesis of mono(p-toluensulfonyl)-βCD. For the chemical modification of the βCD primary ohxydriles, first of all, we synthesized 1-(p-toluensulfonyl) imidazole, as described in the literature [26]. Yield 89%; Rf: 0.57 ($CHCl_3$/MeOH 9:1); 1H-NMR

(300 MHz, $CDCl_3$) d: 8.02 (s, 1H), 7.84 (d, J = 8.4 2H), 7.37 (d, J = 8.4 2H), 7.31 (s, 1H), 7.10 (s, 1H), 2.46 (s, 3H). After that, the βCD was allowed to react with the synthesized 1-(p-toluensulfonyl) imidazole to obtain the 6-O-mono (p toluenesulfonyl)-βCD (tosyl-βCD), in basic media. After one night, the reaction mixture was filtered and a white solid was collected [27,28]. Yield 55%; Rf: 0.37 (iPrOH/H_2O/EtOAc/NH_4OH 5:3:1:1); 1H-NMR (300 MHz, DMSO-d6) d: 7.75 (d, J = 8 Hz, 2H), 7.42 (d, J = 8 Hz, 2H), 5.6–5.8 (m, 14H), 4.83 (br.s, 5H), 4.77 (br.s, 2H), 4.13–4.6 (m, 6H), 3.43–3.76 (m, 28H), 3.15–3.42 (m, overlaps with H_2O), 2.43 (s, 3 H).

For the covalent linking of the activated β-CD (tosyl-βCD), it was added to 4 mL of the concentrated amine-functionalized ultraluminescent gold core–shell nano-emitter (Au@SiO_2-RhB-NH_2) in DMF, or aqueous buffer colloidal dispersion. Thus, it was added to a 5 mM final concentration of tosylated CDs to have a large excess of the modified macrocycle within colloidal dispersions. Moreover, samples with diluted tosylated CDs were applied as well. Dilutions of $\times 10^3$, $\times 10^5$, and $\times 10^6$ were added to control modified cyclodextrins linking on surfaces and diminishing additional multilayered and inter-branching supramolecular structures. In all cases, the reactants were allowed to react for 24 h with continuous agitation. By the application of $\times 10^6$ dilutions, it was estimated that a maximal grafted β-CD concentration of nM would cover all the gold nanosurfaces in the volumes assayed, considering a theoretical calculation with the available total nanosurfaces and surface covered by the smaller ring of the truncated cone shape. During the first hours of reaction times, the reaction vials were sonicated. After the reaction of the β-CD grafting, the NPs were centrifuged at 8500 rpm.

For the luminescence intensity control of the nanoparticles applied, the MEF Enhancement Factor (MEF_{EF}) was determined in the presence of the fluorescent donor reporter at enough concentration to saturate the total theoretical available β-CD grafted over the nanoparticle surface ([Fl] = 40 nM). This factor was determined by the ratio of intensities of ultraluminescent modified β-CD gold core–shell nanoparticles (Au@SiO_2-RhB-CD) and core-less nanoarchitectures ((--)@SiO_2-RhB-CD). The core-less nanoparticles were obtained by using the sodium cyanide leakage method [29] (overnight vortexing of samples was applied in the presence of sodium cyanide to completely digest the metallic core). The MEF_{EF} = [Intensity of Au@SiO_2-RhB-CD/Intensity of (--)@SiO_2-RhB-CD).

At each step in the synthesis, the nanoparticles were centrifuged and redispersed in anhydrous ethanol. Centrifugation was carried out around (8500) rpm, depending on the sample.

The MEF_{EF} was determined by optical excitation of the laser dyes incorporated and gold plasmonics. This was optimized depending on the technique applied. Thus, within colloidal dispersion static fluorescence, and 3D fluorescence was evaluated, while within micro-volumes or from nanostructured deposition on glass slides, Laser Fluorescence Microscopy was used as well.

The 3D fluorescence experiments were carried out varying the excitation and emission wavelengths in the ranges (350–515) nm and (525–690) nm.

The lifetime measurements of nanoparticles and emitters were performed in ethanol. In all the measurements, low concentrations were applied: approximately 5.0×10^8 NPs/mL, which corresponds to a dilution from the concentrated colloidal dispersion, for a dilution factor of 100.

Microscopy conditions applied for nanoimaging were objectives provided by Olympus with oil immersion media with magnification × 100, high Numerical Apertures within 0.75–0.95, and magnifications ×20 and ×60 with air media.

For Laser Fluorescence Microscopy, we applied laser excitation with a Laser Unit of 488.0 and 515 nm Multi-Argon (Sweden). Variable power of irradiance was applied, depending of the concentration of fluorescent reporter and nanoparticle concentration. The objective applied was ×100.

3. Results and Discussion

3.1. Characterization of Multi-Layered Chemical Surface Modifications on Gold Nanoparticles

To synthesize the multilayered gold core–shell nanoparticles, the gold core template to be used was first obtained as a nanoplatform by the modified Turkevich method [30,31] developed by us [32], as described in materials and methods. Thus, 44 nm gold cores (d40 Au NPs) were obtained. This methodology is based on the citrate reduction reaction afforded to homogeneous spherical gold core templates by improving fast and homogeneous agitation. The citrate-stabilized nanoparticles were well-dispersed within aqueous solutions and buffer phosphate pH = 6.99 (Figure 1a); however, within higher polar media such as ethanol, they were less stable and aggregated with the passage of time. The stabilization of gold cores was achieved by PVP polymeric chains used to avoid nanomaterial aggregation within cellular media. The PVP stabilized gold nanoparticles were used for modification by silica shells, applying the Stöber method. Gold core–shell nanoarchitectures were obtained (d40 Au@SiO_2) [33]. In this manner, silica shells @SiO_2 of 5, 15, and 20 nm could be tuned (Table 1), as shown by TEM for 10 nm addition (Figure 1b). These nanoplatforms were modified with a fluorescent shell of RhB, and then covered with an extra few nanometers of protective silica (d40 Au@SiO_2-RhB). Then, these d40 Au@SiO_2-RhB were activated by the addition of amine groups using APS, as modified organosilane that added an additional few nanometers of length to the nanoarchitecture too. At this point, we obtained d40 Au@SiO_2-RhB-NH_2, which afforded the covalent linking of the tosylated CDs. In this manner, we obtained the supramolecular grafted fluorescent gold core–shell silica nanoparticles (d40 Au@SiO_2-RhB-CD). For example, the obtention of nanoarchitectures with silica spacers of 15 nm should be highlighted (Figure 1c), and an additional 2–4 nm were given by the laminated layer and covalently attached supramolecular grafting. In a similar manner, higher spacer lengths were obtained (Figure 1d); however, accurate control of the supramolecular layer was not achieved at this point in the presence of intermediate and concentrated tosylate CDs used. This is mentioned due to the supramolecular addition that could produce additional multilayered depositions by forming from thin shells into inter-branched supra-structures (Scheme 2). The modification with cyclodextrins produced higher interactions between nanoparticles produced by strong hydrogen bridges, and other types of non-covalent interactions were contemplated as well.

Further addition of tosylate cyclodextrins produced inter-crosslinking between macrocycles, forming extra supramolecular shells in the surroundings (Figure 2i) of the d40 Au@SiO_2-RhB that acted as templates of higher-sized assemblies. In this additional supramolecular shell, we noted transparent optical properties that generated color-less structures in comparison to modified fluorescent silica shells. Cyclodextrins showed an absorption band centered in the UV spectrum at 250 nm, accompanied by large transparent intervals of wavelengths. So, it generated a nanoarchitecture core–shell with a strong electroactive gold core surrounded with less contrasted silica shell spacers, while in the case of fluorescent shells, higher contrasted nanoimaging could be detected (Figure 2). However, the cyclodextrin shells were transparent, similar to silica in the absence of highly conjugated organic dyes. In this manner, in presence of concentrated cyclodextrin, conditions were generated for an inter-branched d40 Au@SiO_2-RhB-CD nanoarchitecture with higher optical transparency in comparison to the fluorescent gold core–shell templates (Figure 2ii).

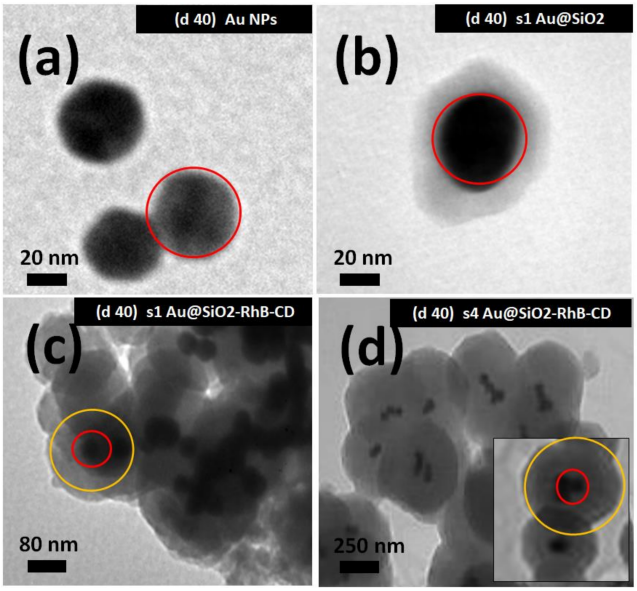

Figure 1. Transmission Electron Microscopy (TEM) imaging of different nanoarchitectures obtained: (**a**) citrate gold nanoparticles stabilized; (**b**) gold core–shell nanoparticles modified with Rhodamine B (RhB) Laser dye (Au@SiO_2RhB) with the addition of the first SiO_2 = 8–9 nm (nominated as Samples s1–2 within short silica spacer lengths); (**c**) multilayered cyclodextrin grafted gold core–shell nanoparticles (Au@SiO_2RhB-CD) with a second spacer shell length of 10–15 nm added for immediately after cyclodextrins grafting; (**d**) Au@SiO_2RhB-CD with a second spacer shell length of 20–25 nm added for immediately after cyclodextrin grafting as well. Note: multilayered cyclodextrin grafted Au@SiO_2RhB-CD showed macrocycle concentrations within a low interval, as described in the materials and methods section.

Therefore, we successfully obtained multilayered cyclodextrin grafted gold core–shell nanoparticles, where each part of the structure was able to tune its emissions and optical properties. It should be noted that the different layers added incorporated consequently varied properties and future interesting perspectives from the chemical and physical point of view. It should be mentioned that gold nanoparticles are optically active nanomaterials, while silica layers and shells are excellent dielectrics and optically transparent materials. In addition, cyclodextrins have a large optical transparent window with the capability to form host–guest complexes as well. Further molecules and short polymeric chains acted as stabilizers, participating in the bottom up. These mentions are to highlight the importance of the definition and stability of the whole based on the participation of all components. Moreover, accurate architecture and well-controlled distances are required as well as within crystals, as Fe_3O_4 nanocrystals and characteristics [34] based on a well-defined magnetic crystal core joined to high-quality GeOx layers developed high resistivity performances. These properties were explained by the well-defined oxygen positions on nanocrystal surfaces. In a similar manner, the modification of well-defined gold nanocrystals surrounded with variable spacer lengths produced variations in their nano-optics shown by different techniques. In a similar manner, it should be mentioned that magnetoelectric coupling in well-ordered epitaxial $BiFeO_3/CoFe_2O_4/SrRuO_3$ heterostructured nanodot arrays also takes place [35]. So, 3D nanoarchitectures accompanied with well-defined atomic positions are highly desired. The nanocristalinity is an important factor that affords to stable, reproducible, and well-performed quantum and optoelectronic properties. The multi-layered gold core–shell nanoarchitectures were characterized as non-porous gold core crystals joined to well-defined supramolecular grafted silica shells that could lead towards controlled variations in their interactions and nanoimaging resolutions. Further studies are intended to evaluate and develop crystalization of different spacer compositions, shells, etc., looking for developments in optically active and transparent micro- and nanobeads. However, at this step of the research, we applied a well-known modified silica methodology

that produced non-porous spacers and well-defined chemical structures. So, with regard to knowing more about the matter composition and properties, we inquired about their stability and dynamics of interactions between them. From these perspectives, we began further spectroscopical studies.

Table 1. [a] Dimensions of multi-layered gold core–shell nanoparticles determined by methods using TEM (Transmission Electron Microscopy) (USA) and DLS (Dynamic Light Scattering) (USA): [a] Lenghts determined experimentally by applied methods; [b] citrate-stabilized gold nanoparticles, [c] gold core–shell silanized nanoparticles, [d] silica shell spacer length, [e] fluorescent gold core–shell nanoparticles, nanoarchitectures, [f] modified organosilane with Rhodamine B (RhB) Laser dye, [g] bilayered gold core–shell silica nanoparticles, [h] modified organosilane with Rhodamine B (RhB) Laser dye linked to second outer silica spacer, [i,j] multilayered cyclodextrin grafted gold core–shell nanoparticles under low and high concentration of macrocycles, [k] colloidal dispersion of fluorescent gold core–shell nanoparticles, [l] standard multilayered cyclodextrin grafted gold core–shell nanoparticles under intermediate concentration of macrocycles.

Method	Structure	Length (Å) [a]	
		S1	**S4**
	Au-cit [b]	45	45
TEM	$Au@SiO_2$ [c]	51–52	70–80
	$(-SiO_2-)$ [d]	6	25
	$Au@SiO_2RhB$ [e]	55	90
	-RhB [f]	3	4
	$Au@SiO_2RhB$- [g]	~70–80	~105–115
	RhB@ [h]	12	14
	$Au@SiO_2RhB$-sCD [i]	100	130
	$Au@SiO_2RhB$-pCD [j]	170	220
	-pCD	50	60
DLS	$Au@SiO_2RhB$ [k]	60	110
	$Au@SiO_2RhB$-CD [l]	224	414

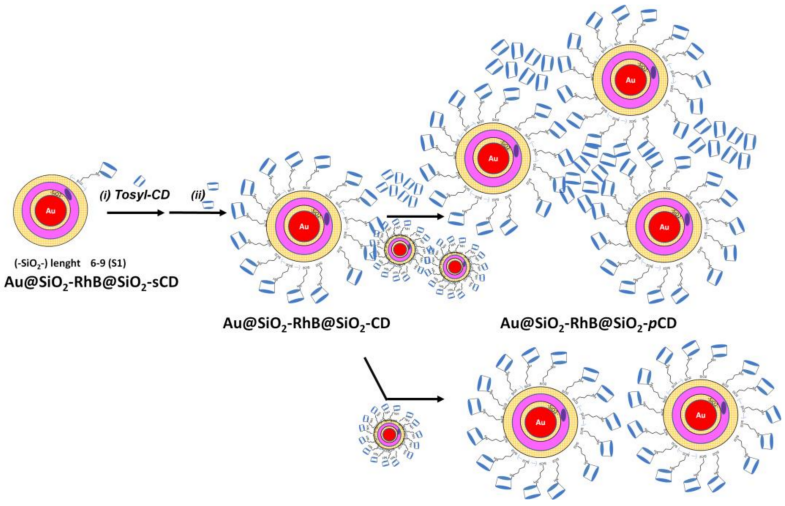

Scheme 2. Schema of assembling and formation of different nano- and micro-multi-layered cyclodextrin grafted gold core–shell nano-arrays ($Au@SiO_2RhB$-CD) and smaller nanoarchitectures. (i) and (ii) are Tosyl-CD multi-step additions. Note: Upper part of schema for per-grafted ($Au@SiO_2RhB$-pCD) and assembled higher nanoarchitectures that were formed; in the lower part are shown nanoarchitectures nominated as single-grafted cyclodextrins of gold core–shell nanoparticles ($Au@SiO_2RhB$-sCD).

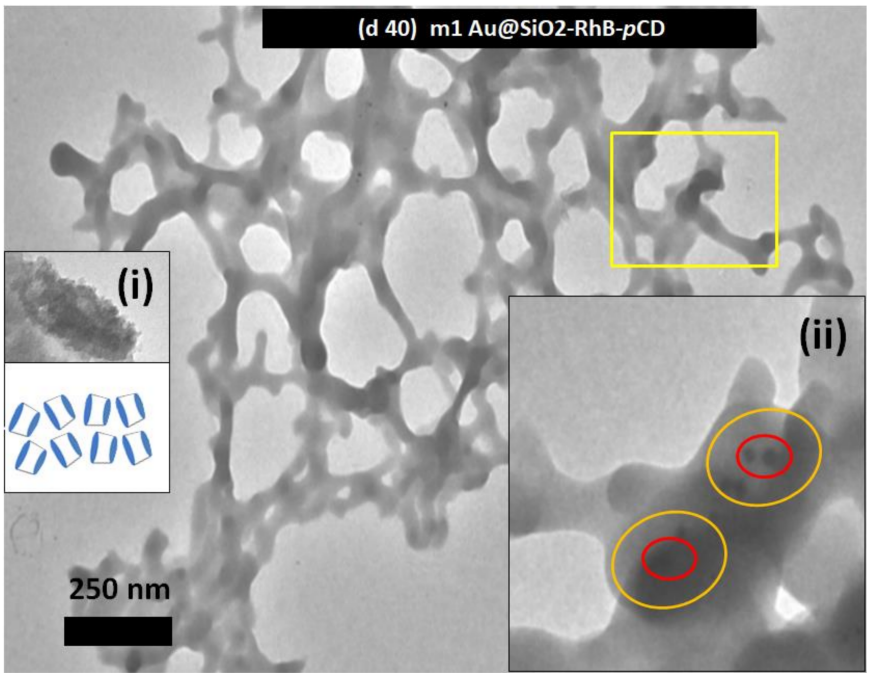

Figure 2. Transmission Electron Microscopy (TEM) imaging of multilayered cyclodextrin grafted gold core–shell nanoparticles with a second spacer shell length of 10–15 nm addedfor immediately after concentrated cyclodextrin grafting application (Au@SiO_2RhB-CD). Insert image (**i**) shows zoomed inter-cross-linking of modified cyclodextrins from inter-branched supramolecular grafted nanoparticles; (**ii**) zoomed inter-branched nanoarchitectures.

3.2. Dynamics and Plasmonics of Multilayered Gold Core–Shell Nanoparticles with Varying Chemical Modifications and Interactions

To evaluate the dynamics and plasmonic developments during nano-interactions, we tracked the development of nano-assemblies from single nanoplatforms d40 Au@SiO_2-RhB-CD with controlled spacer length additions within nanoarchitectures. Thus, we measured light scattering from samples nominated as 1–2 and 3–4, where we incorporated 5–10 nm and 20–25 nm silica spacers, respectively. These were representative results of the control of the nanoscale by the Stöber method of polymerization of organosilanes. The differences between the supramolecular grafted gold core–shell nanoparticles were as minimal as 5 nm, and due to these small variations, we sensed the non-covalent interaction strengths within the nanoscale. Therefore, from sample s1, we observed sizes of 100 nm at times considered as zero or initial within well-dispersed colloidal dispersions. We also recorded, in many samples, higher values, such as 200 nm or even higher, correlated with dimeric and trimetric nanoassemblies. On the other hand, with the passage of time towards 6 and 10 min, values within the interval of 400–600 nm were generated (Figure 3a). Thus, it was noted that measurements at 2 and 6 min were similar; however, sizes were clearly increased up to two times. This trend was similar for samples s1 and 2, with slightly higher interactions occurring, with consequent higher sizes from s1 caused by the smaller size than s2 (Figure 3b). This behavior apparently showed a standard trend of interactions related to relative polar nanosurfaces; however, augmenting their sizes to samples 3 and 4, we also observed increases that were not observed in the absence of the supramolecular grafting. In this context, it was noted that samples s3 and 4 showed similar increments too, but these were associated directly with their sizes (Figure 3c). In particular, we detected in some cases, with s4 samples, larger aggregates within shorter time intervals of measurements, but with the passage of time, only the smaller distribution and differences in sizes were maintained, and this was also recorded from s3 (Figure 3d). Thus, samples s3–4 always occur, forming nano-assemblies from 200 nm centered bands within shorter time scales, while up to 10 min and higher, nano-assemblies up to 800–1000 nm and higher occurred.

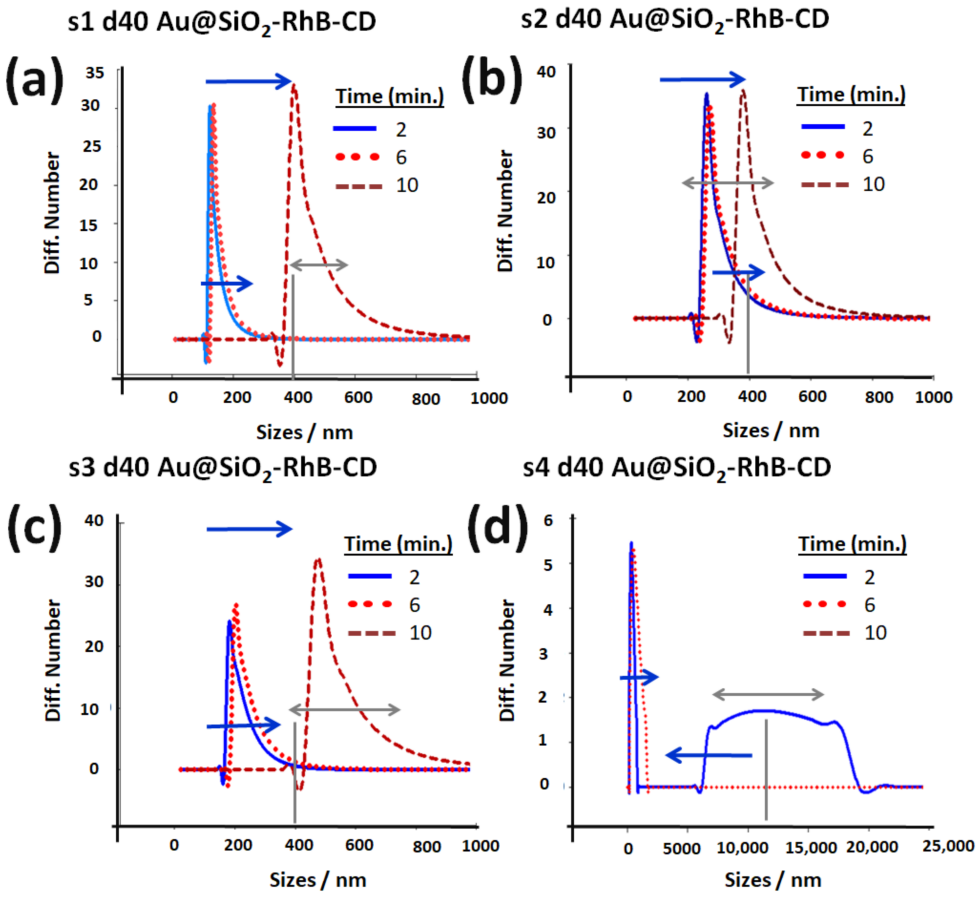

Figure 3. Determinations of sizes with the passage of time by Dynamic Light Scattering (DLS) of multilayered cyclodextrin grafted gold core–shell nanoparticles (Au@SiO_2RhB-CD) of samples: (**a**) s1 with SiO_2 = 6–7 nm; (**b**) s2 with SiO_2 = 8–9 nm; (**c**) s3 with SiO_2 = 15 nm; (**d**) s4 with SiO_2 = 20–25 nm.

In this manner, it was observed that the higher van der Waals interactions generated from smaller sizes were not enough to overcome the diminution of values by increasing sizes (an effect observed previously in the absence of supramolecular grafting) accompanied by higher interaction produced in the presence of highly hydrophilic cyclodextrins. In addition, we clearly observed an apparent lower dispersibility by the appearance of a soft opalescence in the presence of cyclodextrin grafted nanosurfaces in comparison to non-modified core–shell nanoparticles. In this manner, we recorded similar sizes within the same interval of time from silanized samples Au@SiO_2RhB within values of 200–205 nm, while increments from 450 nm to 700 nm in the same interval of time were also detected (Table 2). So, as was observed, the chemical modification with cyclodextrins produced higher interactions, with consequent augmentation of sizes with less contribution from the van der Waals interactions. Even if the cyclodextrin grafted gold core–shell nanoassemblies were able to be re-dispersed, it should be mentioned that samples with grafted cyclodextrins always showed higher nano-assembling than non-grafted and silanized samples.

These observations and explanations from the chemical surfaces and nanoscale control were discussed due to the impact of the consequent nano-optics. It is important to highlight the nanospectroscopy developed from nanoarchitectures with different matter compositions that generate varied signaling. However, even considering the same optical active matter constitution, the sizes, electronic confinement within the nanoscale, and inter-nanoparticle interactions and assembling could generate different optical properties.

For these reasons, then, we evaluated plasmonic properties by absorbance measurements of the different nanoarchitectures. In this manner, we recorded varied behaviors incorporating different chemical modifications. Moreover, the effect of sizes and nanoag-

gregation was observed as well. Citrate-stabilized gold nanoparticles showed a standard plasmon band centered at 537 nm, related to sizes of 40 nm diameter, while the free laser dye RhB showed a centered absorption band at 553 nm. The silica shell addition of red shifted the gold plasmonic band to 545 nm depending on the spacer length added. This spectroscopical characteristic was already observed previously and explained by us as well other authors by an electronic confinement within a dielectric material that modifies the electronic oscillations [36]. In addition, higher sizes and nano-assemblies produce new modes of energy resonances that modify the nanoelectronic and nanoplasmonic characteristics. These effects are explained by modifications in the light scattering of electrons from different shapes and sizes of nanomaterials [37,38]. For these reasons, it is well-known and desired for the evaluation of targeted nanoplasmonic properties and their defined shapes, sizes, and homogenous distributions. The present experiments were conducted on homogeneous colloidal dispersions, but always compared within the same conditions of synthesis corresponding only to one sample related with a silica spacer length.

Table 2. [a] Development of sizes tracked by Dynamic Light Scattering (DLS); [b] assigned number of measurement; [c] time of measurement. Initial time or time zero corresponded to initial well-dispersible colloidal dispersions. [d] Sizes within colloidal dispersions determined by DLS; [e] sizes recorded from distributions of differentials by numbers; [f] sizes recorded from distributions of differentials by intensity recording; [g] gold core–shell nanoparticles with incorporation of Rhodamine B (RhB) Laser dye and controlled silica spacer length addition (Au@SiO_2RhB). Samples nominated as s1 and 2 corresponded to 6–9 and 20–25 nm, respectively. [h] Multilayered cyclodextrin grafted gold core–shell nanoparticles (Au@SiO_2RhB-CD) with incorporation of Rhodamine B (RhB) Laser dye and controlled silica spacer length addition. Samples nominated as s1 and 2 corresponded to 6–9 and 20–25 nm, respectively.

Sample [a]	M [b]	Time [c]/min.	Sizes [d]/$\times 10^3$ nm	
			Diff. n° [e]	Diff. Int. [f]
S1 d40 Au@SiO_2Rh [g]	1	3.00	200	700
	2	6.00	210	590
	3	9.00	205	600
S1 d40 Au@SiO_2RhB-CD [h]	1	3.00	470	3000
	2	6.00	800	150
	3	9.00	650	150
S4 d40 Au@SiO_2Rh [g]	1	3.00	560	3370
	2	6.00	250	610
	3	9.00	260	620
S4 d40 Au@SiO_2Rh-CD [h]	1	3.00	340	630
	2	6.00	350	650
	3	9.00	370	655

Then, supramolecular grafted gold core–shell nanoparticles showed a blue shift of the main plasmonic band accompanied by the generation of a second band towards longer wavelengths centered at 590 and 650 nm (Table 3). These different plasmonic bands were explained by different energy modes related to the main spherical gold plasmonic band modified by multilayers that produced electronic confinement with higher energies within the UV from spherical shapes, while from the formation of nanoassembling, other modes of resonances were generated. As is known, Enhanced Plasmonic (EP) could be produced from close inter-nanoparticle interactions with high electromagnetic field generation [39]. Therefore, samples s1 and 2 showed higher plasmonic intensities (Figure 4) in comparison to s3 and s4, with lower intensities caused by non-optimal silica spacer lengths and higher nanoaggregation related to non-optimal inter-nanoparticle distances. It should be noted that the incorporation of silica on gold nanoparticles added more

dispersible properties in comparison to PEG-stabilized ones obtained previously [40]. In a similar manner, PEG-stabilized gold nanoparticles were modified with cyclodextrins; however, its dispersibility within aqueous media was highly sensitive against media modification such as methanol and ethanol, but in the presence of silica, their dispersibility was conserved in varied apolar solvents as well. This showed the importance of the chemistry of the nanoplatforms where the cyclodextrins were incorporated. Thus, free silanol non-modified with cyclodextrins was mainly responsible for the dispersibility; however, cyclodextrin domains were responsible for nano-assembling. In this manner, it was shown how the tuning of the nanosurfaces could produce different properties generated from different components. It means that in the absence of one of them, the dual properties could not be afforded.

Table 3. Summary of plasmonic properties. [a] Nanoarchitectures modified with varied chemical modifications based on plasmonic gold core templates; [b] hybrid nano-plasmonic bands based on the different optical active material interactions and new modes of energies generated; [c] citrate-stabilized gold nanoparticles; [d] gold core–shell silanized nanoparticles with variable silica spacer shells (@). Samples s1, s2, and s3–4 corresponded to @ lengths of 6, 10, and 20–25 nm; [e] multilayered cyclodextrin grafted gold core–shell nanoparticles based on s1, s2, and s3–4 nanoplatforms.

Nanostructure [a]	**Hybrid Nano-Plasmonic Bands** [b] **/nm**	
	λ1/λ2	λ3/λ4
Au-cit [c]	532	(--)
s1 $Au@SiO_2$ [d]	537	(--)
s2$Au@SiO_2$ [d]	543	(--)
S3–4 $Au@SiO_2$ [d]	550	(--)
s1 $Au@SiO_2$RhB@CD [e]	482/500	569/594
s2$Au@SiO_2$RhB@pCD [e]	483/502	567/593
S3–4 $Au@SiO_2$RhB@CD [e]	397/547	555/600

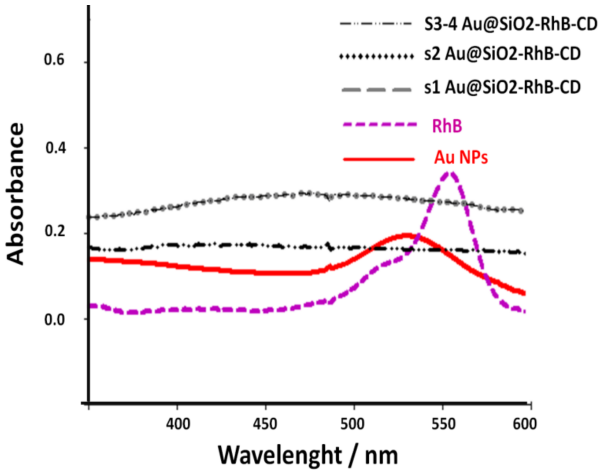

Figure 4. Absorption spectra of different multilayered cyclodextrin grafted gold core–shell nanoparticles (Au@SiO_2RhB-CD) with varied silica spacer lengths @SiO_2. Samples s1, 2, 3, and 4 correspond to 6, 9, 19, and 25 nm. And free RhB and citrate-stabilized gold nanoparticles are overlapped.

To conclude this section, it should be highlighted the importance of the chemical surface modification to tune properties within colloidal dispersions based on their interactions. These interactions modified nano-optics and opened other possibilities related with new modes of energy to related interest in varied research fields.

3.3. Infra-Red Spectroscopic and Microscopy Imaging Characterization

As was observed from the previous section, the importance of interactions and chemical surface modification to modulate dispersibility, interactions, and nano-assembling was highlighted. In these perspectives, and to explain observations, we evaluated interactions between functional groups involved within the different nanoarchitectures. Thus, IR measurements were recorded from colloidal dispersions and drops deposed on silanized glass slides and focused with IR spectroscopical confocal microscopy. In this manner, we recorded clear differences between different chemical surface modifications and functional groups associated (Figure 5). Citrate-stabilized gold nanoparticles showed the most clean spectra; however, we noted that a signal was assigned to the core template within 2750–2960 cm^{-1}. This signal was constant in the other different nanoarchitectures as well. Important differences recorded were highlighted within the stretching of Si-O-Si at 1100 cm^{-1}, accompanied by a variable broad signal in the region of 3100–3600 cm^{-1} related with hydroxyl group stretching. In this region, the main signal associated in this interval of frequencies is observed as well from the literature [41]. Then, the presence of cyclodextrins increased drastically the signaling in the interval of the region of 3110–3600 cm^{-1} and the band centered at 1100 cm^{-1}, associated with different types of hydroxyls such as diol, secondary, and primary groups. The augmentations of the signals were accompanied by shifts in their frequencies towards higher strengths of interactions. In addition, highly intense bands were observed at 1650 and 1450 cm^{-1}, in correspondence with typical bands of amide groups of proteins I and II, which specifically showed stretching C=O, C-N, and bending N-H, respectively.

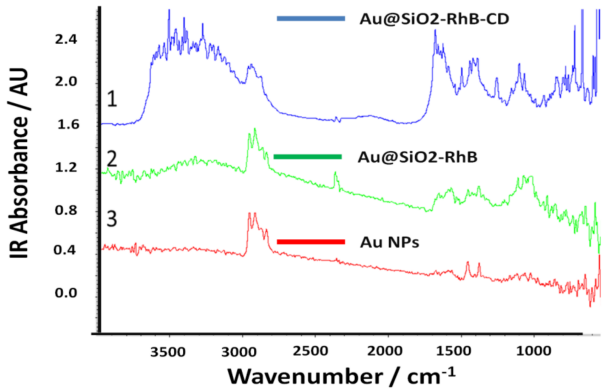

Figure 5. Infrared spectra of different chemical modified gold nanoparticles obtained. Blue line 1 corresponds to multilayered cyclodextrin grafted gold core–shell nanoparticles (Au@SiO_2RhB-CD); green line 2 corresponds to gold core–shell nanoparticles modified with Rhodamine B (RhB) Laser dye (Au@SiO_2RhB) with optimal SiO_2 = 8–9 nm; and red line 3 corresponds to citrate-stabilized gold nanoparticles.

While the most intense bands in the samples were shown at 1650 and 1450 cm^{-1}, which corresponded to typical protein amide bands nominated as I and II, these were assigned to specific stretching of C=O, C-N and bending of N-H, respectively, within the biostructure [42]. In addition, it should be mentioned that we observed an effect of concentration on their interaction strengths and main stretching bands generated from atomic movements and energies involved. However, further studies are in progress to evaluate IR signaling and nano-assembling. In this regard, we observed the samples by IR confocal microscopy to evaluate microscopic patterns related to IR signaling and the formation of nano-assembling. Confocal microscopy imaging generated different micro-assembling explained by the different chemical modifications afforded on nanosurfaces (Figure 6). The different matter incorporated and assembling patterns generated different optical properties in the bright field. Thus, citrate-stabilized gold nanoparticles showed visible dispersibility after sonication; however, within a short period of time, in the standard

time of manipulations of samples for microscopy image recording, a nanoaggregation was produced that occurred at the microscale with high contrast due to the high electroactive properties of gold nanoparticles (Figure 6a), but citrate stabilized nanoparticles very effectively, which permitted the presence of small micro-sized aggregates in the upper limit of the nanoscale with just manual agitation (Figure 6i). Then, the addition of varied silica shells produced higher interactions and nano- and micro-assembling, explained by higher strengths of interactions caused by silanol groups (Figure 6b). These are known as strong interacting and dispersant agents for nanoparticles as well as surfaces. It is important to mention that the addition of silica as an excellent dielectric material and optical transparent material generated visible interstitial volumes between nano-assemblies (Figure 6ii). This optical transparency within the bulk of the nano- and micro-aggregates produced clarity not observed in the aggregated bulk of citrate-stabilized nanoparticles. Finally, we observed, in cyclodextrin grafted nanoarchitectures, higher interaction and micro-assembling (Figure 6c) with visible small nanoaggregates in the limit of diffraction resolution around 250–350 nm (Figure 6iii). We noted optical transparent matter within the nano- and micro-assembling in the presence of higher cyclodextrin grafting and inter-branched nano- and micro-architectures. In this context, to describe these assemblies, we used the term nano- and micro-scales to note the bottom-up effect observed from varied nano-aggregate sizes. Therefore, we recorded by optical IR Microscopy typical sizes of assemblies within 5000–1000 nm with high electron density from citrate gold nanoparticles, while gold core–shell nanoparticles showed average intermediate sizes of 400–600 nm accompanied by interstitial free volumes of 200–300 nm. And cyclodextrin grafted gold core–shell assemblies higher than 10×10^3 nm were observed, with intermediate optical transparency explained by the presence of higher non-optical active inter-branched supramolecular system as spacer lengths of 500–1000 nm (Table 4).

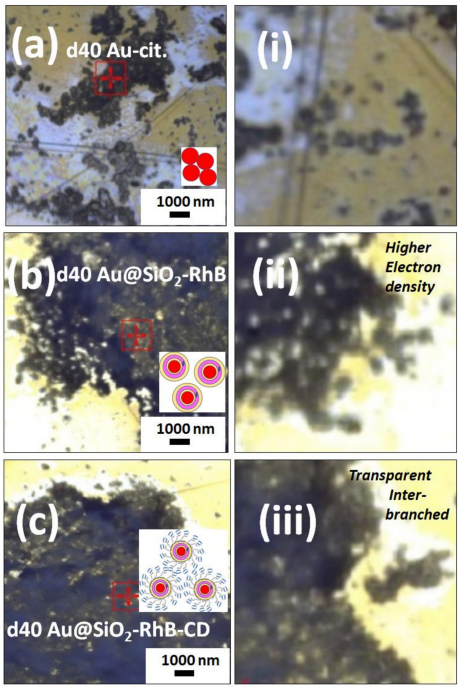

Figure 6. IR Confocal microscopy imaging of different nanoarchitectures obtained: (**a**) citrate-stabilized gold nanoparticles. Inset image (**i**): zoomed images of homogenous nanoparticle detections; (**b**) gold core–shell nanoparticles modified with Rhodamine B (RhB) Laser dye (Au@SiO_2RhB) with optimal SiO_2 = 8–9 nm. Inset image (**ii**): zoomed image focused on intermediate sizes of nanoaggregates with interstitial free volumes detected within the nanoscale; (**c**) multilayered cyclodextrin grafted gold core–shell nanoparticles (Au@SiO_2RhB-CD). Insert image (**iii**): zoomed image of inter-branched and assembled Au@SiO_2RhB-CD with interstitial non-optical active material observed. Other Insert designs are representative nanoarchitectures involucred in the interactions.

So, it is important to remark that there were varied interactions explained by different groups involved that afforded the variable micro-patterns produced from the nanoscale. The nanoscale and pattern observed were different in all the samples and produced visible optical resolution and varied contrasts with consequent internal resolution within the bulk material, permitting by this method inquiry about the internal composition.

Table 4. Imaging characterization by microscopy: [a] nanoarchitectures modified with varied chemical modifications based on plasmonic gold core templates; [b] sizes determined by imaging generated by different microscopy; (*) highlights; [c] optical infrared microscopy; [d] laser fluorescence microscopy; [e] citrate gold nanoparticles; [f] gold core–shell nanoparticles AuO_2-RhB; [g] multilayered cyclodextrin grafted gold core–shell nanoparticles (Au@SiO_2RhB-CD).

Nanostructure [a]	**Sizes/nm (*)** [b]			
	O-IR Microscopy [c]		**Laser Fluo** [d]	
Au-cit [e]	1000–5000 (* High electron density)	(* No apply)	(* No apply)	(* No apply)
Au@SiO_2-RhB [f]	400–600 (* Electron core density + Transparency)	200–300 (* free volumes)	150–250 (* Small dots) 1000 (* Big non-homogeneous distribution))	(* No apply) (* No apply)
Au@SiO_2RhB@CD [g]	>10,000 (* Intermediate Electron density +Transparency)	500–1000 (* Optical Transparency)	400 >5000 (* Resolved Intense dots)	100–200 (inter-branched Nanopatterns)

3.4. Enhanced Luminescence by Multilayered Gold Core–Shell Nanoparticles Applied to Evaluate Inter-Nanoparticle Interactions

Observation of the basal state by different spectroscopical techniques allowed us to record information within colloidal dispersions about physical interactions as well as opto-electronic and plasmonic overlapping. These interactions produced different nanopatterns that raised interest towards the excited state with perspectives on Metal-Enhanced Fluorescence (MEF) phenomena [43]. This perspective was mainly based on the fact that when two or more plasmonic cores interact, they produce coupling near electromagnetic fields between them. This phenomenon could generate Enhanced Plasmonics (EP) properties that could produce higher MEF phenomena from varied nanoresonant patterns.

From these perspectives, first, we evaluated static fluorescence emissions in three dimensions. Thus, 3D fluorescence excites the samples within intervals of excitation wavelengths where there are many interactions involved to generate highly intense MEF emissions. The tiny luminescent gold core–shell nanoparticles showed strong intense emissions centered at 575 nm by optimal excitation wavelength at 535 nm (Figure 7a). This nonclassical light generated was comparable in distribution of excitation and emission wavelengths to previous gold cores of 40 nm; however, the intensity was proportionally diminished to their sizes. This effect should be studied, and actually, there are further studies in progress to elucidate the effect of sizes and inter-nanoparticle interactions. Then, the chemical modification with cyclodextrins and associated nano- and micro-assemblies produced up to 35% higher intensity of emissions (Figure 7b).

The 3D fluorescence showed modified shapes of their emission distributions; however, we detected a light scattering factor produced mainly from inter-branched nano- and microstructures. This important factor should be controlled in order to evaluate MEF Enhancement Factors (MEF_{EF}). So, in regards to evaluating interactions, it was proposed to generate nanoimaging to record more clear and visible information by Laser Fluorescence Microscopy.

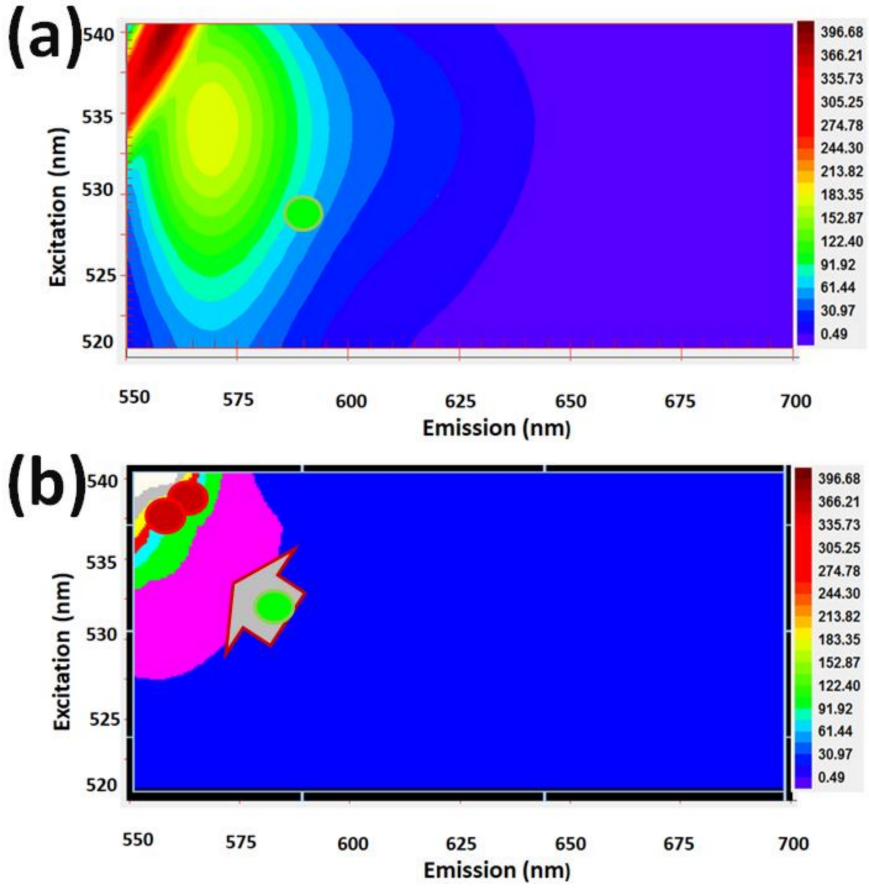

Figure 7. Three-dimensional fluorescence plots and spectral profiles of emission of gold core-shell nanoarchitectures: (**a**) core–shell nanoparticles modified with Rhodamine B (RhB) Laser dye (Au@SiO_2RhB); (**b**) multilayered cyclodextrin grafted gold core–shell nanoparticles (Au@SiO_2RhB-CD). Note: Interval of Emission wavelengths (Δλemis.) were measured between 540 and 700 nm, by an interval excitation of wavelengths (Δλexc.) of 510–550.0 nm. Slits of emission and excitation of 10.0 nm were applied. The narrow indicate high luminescent hot spot with variable intensities explained by the modification of the Nanoarchitecture and assembled state.

In this manner, we observed, in real time, interactions within colloidal dispersions. The previous manipulation drop addition on microscopy glass slides is considered a very good method of dispersion by ultra-sonication. Therefore, it was able to generate small ultraluminescent dots of reduced sizes in close diameter values of Au@SiO_2RhB to determine the absence of photobleaching directly related to MEF phenomena produced within the near field of the nanosurfaces by TEM (Figure 8a). On the other hand, with the passage of time, it produced bigger nanoaggregates of nano-emitters. Thus, single dots below the optical resolution were transformed into spherical nanoaggregates with the side resolution of spherical nanoparticles (Figure 8b). Typical nanoaggregates were determined in the range of 500 nm and 1000 nm. And, when we focused on these nanoaggregates, we were able to estimate smaller shapes interacting to form the aggregate bulk (Table 4). This augmented resolution was permitted by the laser excitation summed with the generation of light from smaller nanoplatforms in comparison to bright field [44].

This was highlighted, even though the technique used was not related to super-resolved Fluorescence Microscopy, where we applied the strategy of the combination of optical setups and emitters incorporated in the sample. In the case of this study, the explanation for the augmented resolution was based on the high sensitivity of the photons generated from reduced sizes within the nanoscale that were able to break down the optical resolution achieved by bright field microscopy given by wavelengths interacting with matter [45].

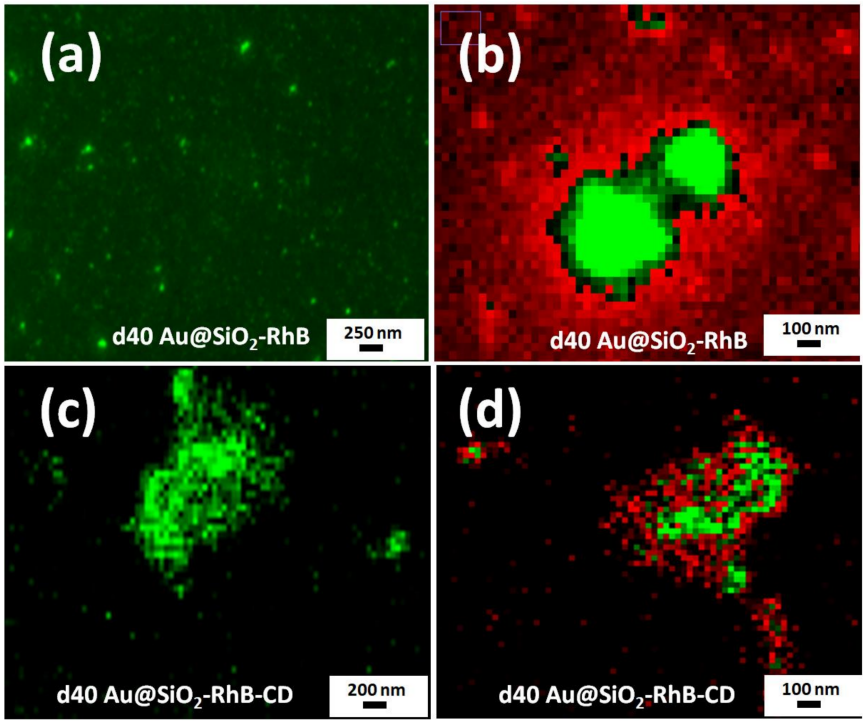

Figure 8. Laser Fluorescence Nanoimaging: (**a**) corresponds to homogenous distribution overview of samples 1–2 of enhanced fluorescent gold core–shell nanoparticles modified with Rhodamine B (RhB) Laser dye (Au@SiO_2RhB) with optimal SiO_2= 8–9 nm. Applied Green LUT; (**b**) zoomed nanoimaging of spherical Au@SiO_2RhB nanoaggregates. Applied Red-Green LUT; (**c**,**d**) nanoimaging overview of samples 1–2 Au@SiO_2RhB-CD applying Green and Red-Green LUT, respectively. Note: Look Up at Table (LUT): parameter adjusting variables such as brightness and contrast. The green colors are associated with higher intensities in the Red-Green LUT.

In contrast, the cyclodextrin grafted nanoarchitecture, in similar concentration conditions, showed a different behavior from the beginning of the manipulation. Higher levels of nanoaggregates were detected related to sizes within the 500–1000 nm interval (Figure 8c). However, we noted an internal resolution that was augmented by the generation of smaller luminescent dots produced from inside the nano-assembly, while similar sizes of non-grafted gold core–shell nanoparticles showed homogenous and highly intense emissions (Figure 8b). The cyclodextrin grafted Au@SiO_2RhB-CD architectures, as recorded by TEM, formed inter-branched spacer lengths that were separated by variable supramolecular spacers. Thus, these samples showed non-overlapping high luminescence intensities; however, smaller sizes with comparably strong interactions given by silanol groups of silanized nanosurfaces provided homogeneous strong luminescence (Table 4). In addition, the closer interactions produced from gold core–shell nanoparticles in the absence of the supramolecular inter-branching permitted inter-nanoparticle coupling due to the fact that their silica spacer lengths of 10–20 nm were in the interval average values to optimize enhancements by Enhanced Plasmonics (EP). This mentioned optimization is of high interest, and in the literature, there are some reports focused on theoretical calculations [46], but not so many experiments [47]. As well, we noted, from supramolecular grafted gold core–shell nanoimaging, different intensities from the whole nano-assembly surfaces by optimizing and adjusting dual-colored imaging parameters (Figure 8d). This observation raised interest in evaluating MEF effects and coupling phenomena, but considering these small highly luminescent dots as close dimensions with single supramolecular grafted gold nanoparticles and potential applications as well.

From the perspective of evaluating inter-nanoparticle interactions and varying chemical surfaces, and we use MEF emissions as a Light Nano-tool for sensing variations in media. It could be varied concentrations and conditions of physical and chemical pertur-

bations such as temperature, shaking, agitation, vortexing, sonication, ultra-sonication, chemical reactions, media modifications, etc. Thus, first, concentration was varied, and we tracked nano-interactions with the passage of time by Laser Fluorescence Microscopy. In this manner, the gold core–shell nanoparticles Au@SiO_2RhB within a low concentration of colloidal dispersions are single small dots with resolutions related to the limit of diffraction of light of 200–300 nm, such as for Bright Field Microscopy, and below this interval of values, the photons produced from nano-platforms are below 100 nm. Therefore, MEF was used as a nano-optical strategy to tune highly intense light that even was conducted through space and time, and their intrinsic final luminescent dots were below confocal expectations. And in many cases, from single-pixel analysis, this led to the estimation of the single and smallest gold core–shell nanoparticles, tuning their multi-layered shells (Figure 9a). The augmentation of colloidal dispersion concentrations produced a higher frequency of small dot ultraluminescent detections (Figure 9b) than lower ones. Moreover, with longer times and concentrations, we recorded augmented strong nano- and micro-aggregates (see Table 4, d15 Au@SiO_2RhB 150–250 assemblies of varied sizes such as small dots, and bigger ones of up to 1000 with nonhomogeneous distribution). However, in these conditions, we recorded higher background intensities in comparison to lower concentrations. These are just mentioned to consider for further applications in Life Sciences, such as for cell labeling, incorporation within cells, tracking luminescent nanoparticles to detect nano-bio-interactions, and other applications based on nanotechnology. In this context, it should be mentioned that there were many developments by conjugating *Eschericcia coli* and gold core–shell nanoparticles with interesting results and further perspectives as well [48].

Then, the supramolecular grafted Au@SiO_2RhB nanoarchitectures naturally showed other behavior, as expected from their targeted interactions by specific organic groups of the macrocycle, and additional polar and van der Waals interactions as well. Thus, these particular interactions, considered as weak non-covalent bonding, showed important implications on the nanoscale. In low colloidal dispersion concentrations accompanied by the application of shaking, we produced very small nano-aggregates related to dimeric and trimetric nano-species (Figure 9c). However, within intermediate and concentrated colloidal dispersion conditions, this was obtained within a few minutes of modification of sizes and shapes (see Table 4, d15 Au@SiO_2RhB-CD assemblies of 400 $>$ 5000, resolved intense dots) that correlated with TEM images (Figure 9d).

In this manner, we noted cyclodextrins as macrocycles that acted as dispersant agents within low concentrations, while towards higher ones, they acted as centers of strong hydrogen bridging with consequent nano-assembling. This assembling or aggregation process could even be in the absence of nanoplatforms. It means that from the molecular and supramolecular level, nanoaggregates could be generated. These nano- and microaggregates showed homogenous highly intensely sized ultraluminescence distribution through the entire volume. We just briefly mention this, and in general, these phenomena are avoided for applications such as analytical chemistry, pharmacy, etc., but they could be controlled by tuning conditions. For this reason, cyclodextrins on nanosurfaces showed important contributions to the inter-nanointeractions. Also, the concentrations added produced visible optical active and non-active properties within nano- and micro-architectures.

In addition, cyclodextrins grafted on different spacers related to different optical properties afford the resolution of new nano-optics as well. In this context, we note the chemical properties of molecules and their effects on physical properties. This is the case of quantum dots stabilized by different stabilizing agents that could tune their excited semiconductive states. In the case of gold core–shell nanoparticles, the chemistry applied on metallic nanoparticles also affects the plasmonic properties and MEF. So, molecules produce chemical inter-phases that tune opto-electronic properties, electronic oscillations, and logically final nano-optical properties. But chemical inter-phases not only affect physical properties directly, they also affect interactions between inter-nanoparticles, producing or generating other modes of electronic resonances based on the formation of nanoassemblies as new

material in comparison to individual nano-components. In this context, it highlighted differences in how non-classical light is delivered from gold cores of 40–50 nm diameter, depending on the types of spacers and interactions produced between them. Cyclodextrin gold core–shell nanoparticles were modified with short polymeric chains produced from single nanoemitters to larger nanoassemblies with bright and stable emissions [49]. These nanoemitters produced less light delivery, controlled by the quantity of the RhB Laser dye added, as well as by the lack of optical material to transfer the light through space and time [50]. So, from the point of view of nano-optic resolution, it generated high-performance nano-optics, but focusing on the power of irradiancy, it was lower than gold nanoparticles modified with silica spacers shells. Silica spacer shells could act as excellent media to transfer light such as occurs within waveguides. Thus, in this research work, we produced highly intense nanoemitters that could be tuned towards single nano-emitter tuning, controlling additional layers and chemical functionalizations [51,52].

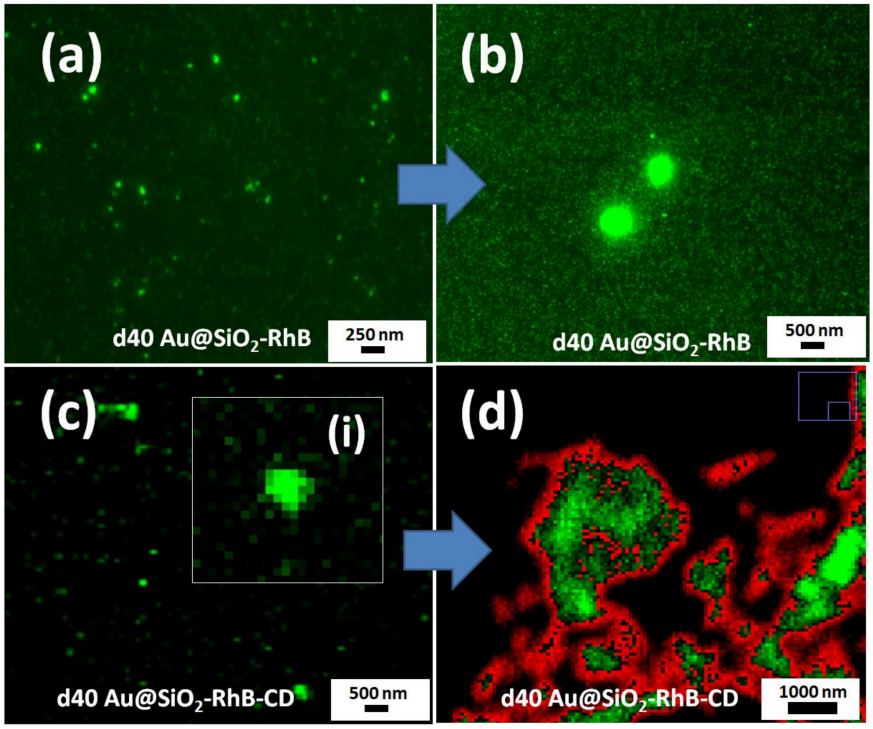

Figure 9. Laser Fluorescence Nanoimaging (**a**,**b**) corresponds to samples 1–2 of Enhanced Fluorescent gold core–shell nanoparticles modified with Rhodamine B (RhB) Laser dye (Au@SiO_2RhB) with optimal SiO_2 = 8–9 nm in diluted and concentrated conditions, respectively, and (**c**,**d**) samples 1–2 grafted Au@SiO_2RhB with cyclodextrins (CDs) in diluted and concentrated conditions, respectively (Au@SiO_2RhB-CD). Note: Look Up at Table (LUT): parameter for adjusting images by variables such as brightness and contrast. Applied Red-Green LUT: 543 nm laser excitation applied. The green colors are associated with higher intensities in the Red-Green LUT.

These examples are first observations, with potential perspectives for further developments focused on different and varied optical setups, miniaturized instrumentation, and nanotechnology. In these perspectives, In Flow methodologies are actually of high interest; therefore, in the next and first step, looking for further knowledge towards applied approaches, we evaluated these previous nanoarchitectures within cytometer with varied laser excitations.

3.5. Tuning in Flow Enhanced Nano-Optics

In order to evaluate enhanced nano-optical setups such as MEF based on gold core–shell nanoarchitecture, it was passed through an In Flow Cytometer system with varied

laser applications to detect light scattering and fluorescence events. In this manner, we were able to evaluate (i) inter-nanoarchitecture interactions, (ii) assembling, (iii) non-classical light generation from the nanoscale under continuous movement, (iv) nanoarchitecture, (v) nanosurface modifications, (vi) effect of sizes, (vii) further plasmonic effects from the presence and absence of the gold cores, and (viii) Enhanced Plasmonic coupling as well from their interactions. Interaction between plasmonic gold cores and core-less nanoarchitectures was contemplated. These are mentioned just to highlight the interest and potential results recorded from the experimental dataset proposed, considering that in all cases, quantifications of effects, counting, and further analytical information were expected. The generation of multi-modal energies from confined nanoplatforms showed potential interest for developments where tracking nanoplatforms and variations in their conformation or surrounding media is required.

In this context, cytometry techniques permitted us to record light scattering and related parameters to obtain different information from the nano- and microstructure. Thus, we obtained two parameters known as side-scattered light (SSC) and forward-scattered light (FSC). Distributions of both parameters were generated by applying laser excitations at 488 nm and 555 nm with different filters to record signaling in different wavelength intervals of values. Thus, we assigned D1 with blue and D2 violet color distributions, respectively, for the mentioned order of laser excitations. In addition, by switching the detection system and positions of them, we recorded the fluorescence emission and detection events from nano- and micro-emitters passing through the In Flow system.

Thus, first, it was characterized by gold core–shell nanoparticles Au@SiO_2RhB and supramolecular grafted nanoarchitectures Au@SiO_2RhB-CD. In this manner, we recorded from samples s1 and s2 Au@SiO_2RhB a low and hidden D1 SSC distribution accompanied by a higher overlapped and visible detection of D2 (Figure 10a) within an interval of values such as 5–10 $\times$ 10^3 (D1) and 10–100 $\times$ 10^3 (D2), respectively. On the other hand, the FSC parameter values were detected in low numbers and frequency within longer intervals of values for D1, such as within 50–150 $\times$ 10^3; however, small distribution intervals around 5–10 $\times$ 10^3 for D2 were detected. Then, samples s3 and s4 of Au@SiO_2RhB, related with bigger nanoarchitecture and less nanoaggregation, showed strong centered D1 distributions within 5–25 $\times$ 10^3, while D2 showed a completely different behavior in comparison to s1–s2 (Figure 10b). Therefore, smaller diameters were correlated with consequent higher detections of D2 distributions related to filter within the IR interval of wavelengths. As is known, the development of nanoassemblies produces other modes of energies detected in the IR interval from many synthetic and biological systems (Figure 10a). On the other hand, the augmentation of sizes lowered interactions and aggregation states that afforded the disappearance of D2 distributions (Figure 10b).

After cyclodextrin modification of gold core–shell nanoparticles, the distributions recorded were completely different in comparison to non-grafted gold core–shell nanoparticles. So, samples s1–s2 of Au@SiO_2RhB-CD showed very low aggregation behavior (Figure 10c) in the conditions assayed, as also recorded by Laser Fluorescence Microscopy. Samples s1–2 showed smaller distributions of D1 and D2 as well, while s3–4 showed longer intervals of values for both SSC and FSC (Figure 10d). These observations were correlated with well-dispersed colloidal dispersions in the presence of minimal nano-aggregation. However, higher diameters in the presence of additional non-covalent interactions provided by cyclodextrins permitted the formation of stronger nano-assembling. but, it should be noted that s1–2 augmenting concentrations led to higher distributions of light scattering parameter detections. We mention this just to note that by this technique, it was possible to correlate similar trends in comparison to other ones applied. In this context, it does not mean that the same information was recorded, but in this case, interpretations based on different energy modes permitted us to arrive at the construction of similar models of the colloidal state from single nanoarchitecture interactions.

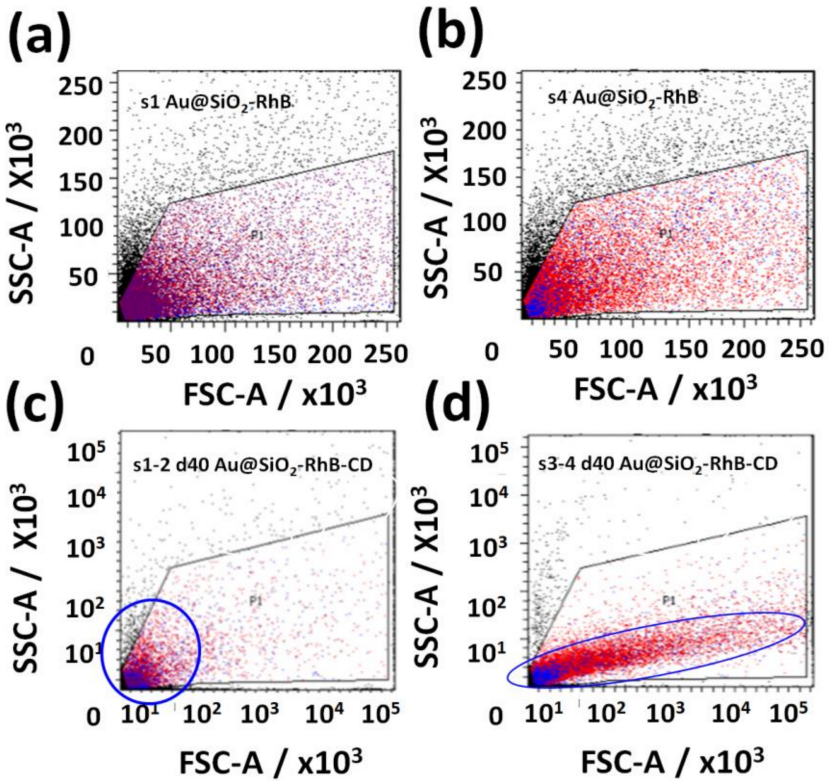

Figure 10. Analysis of contour plots of side-scattered light, SSC (SSC is proportional to cell granularity or internal complexity) vs. forward-scattered light, FSC (FSC is proportional to cell surface area or size) of core–shell nanoarchitectures. Laser excitations at 488.0 nm and 555.0 nm with emission filters at 530/30 nm and 585/42 nm, for Alexa Fluor 488-A vs. AF555-A, respectively (D1 = blue distribution recorded with 488.0 nm laser excitation; and D2 = violet distribution with 555.0 nm excitation); (**a**,**b**) samples 1–2 and 3–4 of fluorescent gold core–shell nanoparticles modified with Rhodamine B (RhB) Laser dye (Au@SiO_2RhB) with SiO_2= 6–9 nm and 20–25 nm, respectively; (**c**,**d**) samples 1–2 and 3–4 correspond to grafted Au@SiO_2RhB with cyclodextrins (CDs), respectively, nominated as multi-layered cyclodextrin grafted gold core–shell fluorescent nanoparticles (Au@SiO_2RhB-CD).

In this regard, it should be mentioned that the contour plots of side-scattered light (SSC) vs. forward-scattered light (FSC) were previously applied for nano- and micro-sized optical active and non-optical active materials from synthetic and biological sources. In this manner, it was highlighted that SSC is a measurement of mostly refracted and reflected light that occurs at any interface within the particle, biostructure, or cell, where there is a change in refractive index [53]. The SSC is collected at approximately 90 degrees to the laser beam by a collection lens and then redirected by a beam splitter to the appropriate detector. Thus, the SSC parameter is proportional to cell granularity or internal particle complexity. The FSC provides a suitable method of detecting particles greater than a given size, independent of their fluorescence, and it is therefore often used in immune phenotyping to trigger signal processing [54]. Thus, well-dispersible nanoplatforms permitted the detection of Single Fluorescent detection events with variable distributions and frequencies within SSC vs. FSC contours plots, and permitted as well the detection of aggregation of particles and interactions between components. So, even if this technique is not able to determine sizes, it could be discussed in the context of the developments of varied sizes from nano- to micro-aggregates. In addition, based on the laser technique and dual detection systems, we are able to obtain information about their optical active components, and in this manner, about the nano- and micro-optical particle characteristics. These are general comments about the state of the art of knowledge of the technique for nano-optics analysis.

From these perspectives, and to evaluate enhancements based on MEF, as was previously stated, the core-less nanoarchitecture in the absence and presence of grafted

supramolecular systems was passed through the system. The core-less nanoarchitectures were obtained as described in the material and methods by digestion of their gold core with the addition of sodium cyanide accompanied by shaking and sonication. Thus, the SSC vs. FSC plots showed drastic differences in detection events by passing through the core-less nanoarchitecture in the absence of grafted supramolecular systems (--)@SiO_2RhB (Figure 11a) and in the presence of grafting (--)@SiO_2RhB-CD (Figure 11b). It recorded the complete elimination of the strong and well-defined detection events recorded at different excitation wavelengths (Figure 11a,b) in comparison to the presence of core templates (Figure 10). The distribution of core-less nanoarchitectures showed similar patterns for non-grafted and supramolecular grafted nanoarchitectures, respectively (Figure 11a,b).

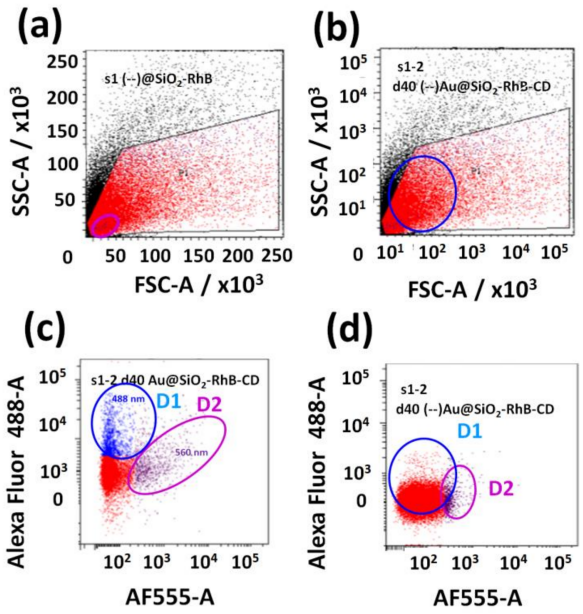

Figure 11. In flow analysis of core-less nanoarchitectures: (**a**) analysis of contour plots of samples 1–2 of fluorescent gold core-less nanoarchitectures modified with RhB ((--)@SiO_2RhB) by side-scattered light, SSC (SSC is proportional to cell granularity or internal complexity) vs. forward-scattered light, FSC (FSC is proportional to cell surface area or size). Laser excitations at 488.0 nm and 555.0 nm with emission filters at 530/30 nm and 585/42 nm, for Alexa Fluor 488-A vs. AF555-A, respectively (D1 = blue distribution recorded with 488.0 nm laser excitation, and D2 = violet distribution with 555.0 nm excitation); (**b**) contour Plots of SSC vs. FSC of multilayered cyclodextrin grafted fluorescent core-less nanoarchitectures ((--)@SiO_2RhB@CD); (**c**,**d**) In Flow Fluorescence event detection of samples 1–2 multilayered cyclodextrin grafted core–shell (Au@SiO_2RhB-CD) and core-less nanoarchitectures ((--)@SiO_2RhB-CD), respectively.

Then, to quantify enhanced phenomena, we defined the ratio of counting NPs between core–shell and core-less nanoarchitectures in the presence of grafted supramolecular (Rccd) and non-grafted (Rcc) nanoarchitectures applied, respectively. These ratios were determined with both lasers applied. Thus, we recorded luminescent detection events by 488 nm and 555 nm laser excitations in the presence of the supramolecular grafted gold core templates (Figure 11c) and core-less nanoarchitectures (Figure 11d). In this manner, we found Rccd of 100 and 90 for samples s2 and 4, respectively, by 488 nm laser excitation, and 2.0 and 1.5 by 555 nm excitation as well (Table 5). Moreover, from non-grafted supramolecular nanoparticles nominated only as core–shell nanoarchitecture Au@SiO_2RhB, the Rcc values were 50 and 25 for samples s2 and 4, respectively, by 488 nm laser excitation, and 20.0 and 10.0.5by 555 nm excitation, respectively, as well (Table 5).

Table 5. Summary of In Flow data: [a] laser excitation applied for tracking nanoparticles (NPs), [b] sample nominated as 2 and 4 corresponding to s2 and s4 with SiO_2 spacer shell lengths of 9–10 nm and 20–25 nm, respectively, [c] In Flow NPs counting $\times 10^3$ unities, [d] and [e] ratio of counting NPs between core–shell and core-less nanoarchitectures in presence of grafted supramolecular (Rccd) and non-grafted (Rcc) nanoarchitectures applied, respectively, [f] multilayered cyclodextrin grafted gold core–shell nanoparticles (Au@SiO_2RhB-CD), [g] multilayered cyclodextrin grafted core-less nanoarchitectures ((--)@SiO_2RhB-CD), [h] gold core–shell nanoparticles Au@SiO_2-RhB, [i] core-less nanoarchitectures (--)@SiO_2-RhB.

Laser Exc./nm [a]	Sn [b]	In Flow Nano-Counting/$\times 10^3$ [c]				Rccd [d]	Rcc [e]
		Au@SiO_2RhB -CD [f]	(-)@SiO_2 RhB -CD [g]	Au@SiO_2 RhB [h]	(-)@SiO_2 RhB [i]		
488	S2	2000	20	1950	450	100	50
	S4	1600	17	900	35	90	25
560	S2	800	500	850	29	2	20
	S4	650	420	730	67	1.5	10

3.6. Discussion and Perspectives of Multilayered Gold Core–Shell Nanoarchitectures for Optical Active Nanoplatforms

From these results, we highlighted augmented counting from core–shell nanoplatforms in comparison to core-less nanoarchitectures. These recordings were expected by free Au@SiO_2RhB, as also obtained previously by us; however, the effect of the chemical modification with cyclodextrins on the nanosurface was not evaluated on fluorescent silica shells nominated as Au@SiO_2RhB-CD nanoarchitecture in the present research work. This effect within optimal colloidal dispersion conditions of concentration and interactions showed up to 100 times the Rccd values, accompanied with stable well-defined distributions of light scattering detection events and by fluorescence as well that showed different degrees of developments of nano- and micro-assemblies correlated with varied sizes. These variations were detected from controlled spacer length additions on the nanoarchitecture as well as modifying their chemical surface with different spacer lengths and chemical surface modifications by cyclodextrins. In this manner, we developed a nanoscale control and non-classical light tuning method able to be detected by different spectroscopical, microscopy, and In Flow detection techniques. In this context, it should be mentioned and highlighted that the particular properties were developed from single nanoarchitectures, applying nanochemistry within colloidal dispersions. These are some of the many challenges to face in the next generation of nanotechnology with perspectives focused on life sciences reagents. On particles, standard nano- and microbeads within fluidics systems, nanolabellers, etc., can be included.

4. Conclusions and Future Perspectives

In this research work, we showed multilayered chemical modifications by adding variable types of matter compositions on gold core templates. Variable silica shell lengths were added to separate fluorescent modified organosilanes from the gold cores, followed by the addition of a few nanometers of protective silica layers and an additional extra second silica spacer shell to set up nanoplatforms in the presence of mined sites ready to link activated cyclodextrin macrocycles. In this manner, we obtained a multilayered gold core–shell nanoarchitecture with varied optical properties within each layer added. In this context, we evaluated the sensitivity of the developed nano-optical platform by varied spectroscopical, microscopical, and flow detection techniques. Metal-Enhanced Fluorescence phenomena with intrinsic stable and high-intensity emissions afforded varied nanoemitter patterns based on different interactions between them, depending on the chemical surface

modifications applied. In addition, we evaluated light scattering signaling within colloidal dispersions under continuous movement. Thus, we achieved accurate control of the nanoarchitectures permitted by TEM. Gold core templates of 45 nm diameter were modified with an average of 10 nm silica spacer shells with 3–4 nm fluorescent shells. The supramolecular systems were covalently linked and afforded augmented inter-nanoparticle interactions, depending on colloidal dispersion concentrations and cyclodextrin concentrate added on the nanosurfaces. We observed the generation of a supramolecular intercross-linked additional layer when we added higher concentrations of this type of activated macrocycle by SN_2 reactions. Varying concentrations of the supramolecular grafted gold core–shell nanoparticles were observed from single nanoemitter detections to larger nanoassemblies. Intermediate concentrated nanoassemblies permitted the resolution of individual nanoemitters within nanoassemblies. On the other hand, the non-grafted supramolecular core–shell nanoarchitecture produced high ultraluminescent nanoaggregates without resolution within the nanostructured assembly of micrometer size. However, the free gold core–shell nanoparticles within lower colloidal concentrations showed highly intense nano-emissions, stable with the passage of time, with interesting perspectives for immune ultraluminescent nanolabelling and related research fields.

So, as expected, interactions and assembling, from the supramolecular to the nanoscale and beyond, varied. However, based on MEF, by tuning multi-layered gold core templates with different optical properties incorporated, varied nano-optics were afforded, highlighting the following facts. (i) The addition of non-optical active supramolecular macrocycles produced within the bright field transparent regions permitted tuning of emissions from micro-assembling with single nano-resolutions recorded from ultraluminescent gold core–shell nano-templates. (ii) The incorporation of grafted supramolecular systems provided additional strong hydrogen bonding that, within concentrated colloidal dispersions, produced homogeneous highly intense luminescent colloidal dispersions and surfaces. The intensities were not the higher ones in comparison to non-grafted nanoparticles; due to the inter-grafted layers formed, they were not yet optimized for EP and MEF. However, it showed proof-of-concept supramolecular interactions and spacing between inter-nanoparticles. (iii) Moreover, it highlighted intercross-linking of supramolecular shell formations and inter-branched nano-architecture by varying concentrations of macrocycles and colloidal dispersions as well.

About nanoimaging, as was expected, the shapes from the bulk were correlated between TEM and Laser Fluorescence Microscopy; however, the non-classical light generated was propagated through space and time, adding augmented sizes of up to 35% and increased diameters accompanied by increased background as well.

Thus, the different nanoarchitectures obtained and compared by different techniques and methods show the potential for interesting and varied types of further studies and applications. In this context, it is important as well to mention that the bottom-up method achieved was based on wet chemistry and colloidal dispersion manipulations. Therefore, these are chemical methods that, from the point of view of scale-up and nanomaterial manufacturing, are of high interest for a wide range of applications. However, depending on the targeted use, physical techniques and methods to design and fabricate nanoarchitectures should also be considered [55]. In many cases, it is possible to tune the same design but not always the same effect, due to the differences in the final nanomaterial supporting media. Physical techniques could produce highly accurate designs and crystals, but wet chemistry, overcoming problems within organized media, could provide homogeneous colloidal dispersions [56]. So, both methodologies today could be considered to create new nano-optics approaches, testing new properties, physical and chemical phenomena, metamaterial conformations, and further applications [57].

In this regard, and from the perspective of testing nano-optics within In Flow optical setups, for example, we evaluated in this research work In Flow Cytometry with dual excitation and detections based on light scattering and fluorescence. Thus, we recorded varied distributions on detection events, depending of conditions, nanoarchitecture, assembling,

and laser application. Thus, we noted the capability to detect nano- and micro-aggregation by light scattering, which is explained by single non-covalent interactions at the molecular level applied on nanosurfaces. Moreover, we were able to record enhanced nano-optics based on MEF that afforded improve performances in their counting. In the presence of supramolecular grafted gold core–shell nanoplatforms, it was determined that 100 times more detection events occurred, in comparison to core-less nanoarchitectures. So, in this case, the light scattering component afforded these enhanced detections, based on core–shell nanoparticles with resonant assembling from the bulk under continuous movement. But by Laser Fluorescence nanoimaging, it was not as high as expected. However, up to a 25% increase was generated. In this manner, MEF Enhancement factors and Fluorescence Resonance Energy Transference (FRET) phenomena are under study as well. In addition, further studies are in progress to evaluate them for molecular detections using macrocycles as host receptors covalently linked to nanosurfaces and forming nano-assembling within colloidal dispersions and modified surfaces as well.

Author Contributions: The following contributions were made by each co-author. M.R.R. worked on the IR experimental data recording, analysis and discussion; A.V.V. participated in the work related with supramolecular structures and interactions in the nanosurfaces achieved; M.V.A. worked in the collective analysis of synthetic nanoarchitectures and unicellular microorganism interactions; and A.G.B. worked in the supervision of Luna R. Gomez Palacios, design, conceptualization of the nanoarchitecture, focusing the attention as Director of his ongoing research projects associated with nanophotonics, biophotonics and nanomedicine in collaboration with international research partners. All authors have read and agreed to the published version of the manuscript.

Funding: This research was funded by SECYT-UNC. Title: "Synthesis and Characterization of new highly fluorescent supramolecular nanostructures applied to diagnostics by nanoImaging". Director: Dr. Guillermo Bracamonte (Accepted-Code 30820150100057CB, Res. SECyT 366, June 2016–July 2026). The APC was funded by Crystals, MDPI.

Data Availability Statement: The data, supporting results, and reported results in general can be provided by the author upon request.

Acknowledgments: We greatly thank the grants and funds provided to carry out this work. We would also like to thank to SeCyT (Secretary of Science and Technology from the National University of Cordoba, UNC, Argentina) for the Grant for Young Researchers awarded to A.G.B. We also thank Paula Abadie and Pilar Crespo for their assistance, from the Laboratory of Cytometry, Research Center of Biochemistry and Immunology, Department of Biochemistry, National University of Cordoba, Argentina (Centro de Investigaciones en Bioquímica Clínica e Inmunología, CIBICI-CONICET). Moreover, we greatly acknowledge the visit to Jesse Greener Laboratory, in the Département de Chimie forming part of the CQMF (Quebéc Center for Functional Materials) and CERMA (Center for Research on Advanced Materials), at Université Laval, Québec, Canada, and the discussions held about the design of microfluidic and bio-analytical techniques. In a similar manner, we are grateful to Denis Boudreau from the Département de Chimie and Centre d'Optique, Photonique et Laser, Université Laval, Québec, Canada, for collaborative research work in progress related to nanophotonics and biophotonics, as well as to all the Canadian grants received during the postdoctoral position held by the corresponding author.

Conflicts of Interest: The authors declare no conflicts of interest. Moreover, it is stated that the funders had no role in the design of the study; in the collection, analyses, or interpretation of data; in the writing of the manuscript; or in the decision to publish the results.

References

1. Bracamonte, A.G. Gold nanoparticles chemical surface modifications as versatile Nanoplatform strategy for fundamental Research towards Nanotechnology and further applications. *Nanosci. Nanotechnol.* **2022**, *1*, 1004.
2. Salinas, C.; Amé, M.; Bracamonte, A.G. Tuning silica nanophotonics based on fluorescence resonance energy transfer for targeted non-classical light delivery applications. *J. Nanophotonics* **2020**, *14*, 046007. [CrossRef]
3. Zhuang, Y.; Ren, X.; Che, X.; Liu, S.; Huang, W.; Zhao, Q. Organic photoresponsive materials for information storage: A review. *Adv. Photonics* **2020**, *3*, 014001. [CrossRef]

4. Hutchinson, W.; Bracamonte, A.G.; Sahai, N. Electronic properties and Pseudo-Electromagnetic Fields of Highly Conjugated Carbon Nanostructures. *Curr. Mater. Sci.* **2022**, *15*, 204–214. [CrossRef]
5. Salinas, C.; Bracamonte, G. Design of Advanced Smart Ultraluminescent Multifunctional Nanoplatforms for Biophotonics and Nanomedicine applications. *Front. Drug Chem. Clin. Res.* **2018**, *1*, 1–8. [CrossRef]
6. Bracamonte, A.G. *Frontiers in Nano and Micro-Device Design for Applied Nanophotonics, Biophotonics and Nanomedicine*; Bentham Science Publishers Ltd.: Sharjah, United Arab Emirates, 2021; Chapters 1–15, ISBN 9781681088563.
7. Bracamonte, A.G. Advances in Quantum properties of Graphene applied for targeted functional Nanomaterials and Metamaterials. *Recent Prog. Mater.* **2023**, *5*, 1–17.
8. Lessard-Viger, M.; Brouard, D.; Boudreau, D. Plasmon Enhanced energy transfer from a conjugated polymer to Fluorescent core shell Nanoparticles: A photophysical study. *J. Phys. Chem. C* **2011**, *115*, 2974–2981. [CrossRef]
9. Palacios, L.R.G.; Bracamonte, A.G. Generation of Bioimaging towards design of hybrid micro-machines and micro-swimmers. *J. Chem. Res. Adv.* **2022**, *3*, 22–27.
10. Palacios, L.R.G.; Bracamonte, A.G. Development of Nano-, Microdevices for the next generation of Biotechnology, Wearables and miniaturized Instrumentation. *RSC Adv.* **2022**, *12*, 12806–12822. [CrossRef]
11. Lakowicz, J.R. Radiative Energy Engineering 5: Metal enhanced fluorescence and plasmon emission. *Anal. Biochem.* **2005**, *337*, 171–194. [CrossRef]
12. Asselin, J.; Legros, P.; Grégoire, A.; Boudreau, D. Correlating Metal-Enhanced Fluorescence and Structural Properties in Ag@SiO_2 Core-Shell Nanoparticles. *Plasmonics* **2016**, *11*, 1369–1376. [CrossRef]
13. Bondre, N.; Zhang, Y.; Geddes, C.D. Metal-Enhanced Fluorescence based Calcium Detection: Greater than 100-fold increase in signal/noise using Fluo-3 or Fluo-4 and Silver Nanostructures. *Sens. Actuators B* **2011**, *152*, 82–87. [CrossRef]
14. Golberg, K.; Elbaz, A.; McNeil, R.; Kushmaro, A.; Geddes, C.D.; Marks, R.S. Increased Bioassay Sensitivity of Bioactive Molecule Discovery using Metal-Enhanced Bioluminescence. *J. Nanoparticle Res.* **2014**, *16*, 2770. [CrossRef]
15. Puchkova, A.; Vietz, C.; Pibiri, E.; Wünsch, B.; Paz, M.S.; Acuna, G.P.; Tinnefeld, P. DNA Origami Nanoantennas with over 5000-fold Fluorescence Enhancement and Single-Molecule Detection at 25 µM. *Nano Lett.* **2015**, *15*, 8354–8359. [CrossRef]
16. Lackowicz, J.R. Radiative Decay Engineering: Biophysical and Biomedical Applications. *Anal. Biochem.* **2001**, *298*, 1–24. [CrossRef] [PubMed]
17. Geddes, C.D.; Lackowicz, J.R. Editorial: Metal-Enhanced Fluorescence. *J. Fluoresc.* **2002**, *12*, 121–129. [CrossRef]
18. Viger, M.L.; Live, L.S.; Therrien, O.D.; Boudreau, D. Reduction of self-quenching in fluorescent silica-coated silver nanoparticles. *Plasmonics* **2008**, *3*, 33–40. [CrossRef]
19. Rioux, M.; Gontero, D.; Veglia, A.V.; Bracamonte, A.G.; Boudreau, D. Synthesis of Ultraluminiscent gold core-shell Nanoparticles as NanoImaging Platforms for Biosensing applications based on Metal enhanced fluorescence. *RSC Adv.* **2017**, *7*, 10252–10258.
20. Veglia, A.V.; Bracamonte, A.G. β-Cyclodextrin grafted gold nanoparticles with short molecular spacers applied for nanosensors based on plasmonic effects. *Microchem. J.* **2019**, *148*, 277–284. [CrossRef]
21. Kimling, J.; Maier, M.; Okenve, B.; Kotaidis, V.; Ballot, H.; Plech, A. Turkevich Method for Gold Nanoparticle Synthesis Revisited. *J. Phys. Chem. B* **2006**, *110*, 15700–15707. [CrossRef]
22. Lessard-Viger, M.; Rioux, M.; Rainville, L.; Boudreau, D. FRET enhancement in multilayer core-shell nanoparticles. *Nano Lett.* **2009**, *9*, 3066–3071. [CrossRef] [PubMed]
23. Graf, C.; Vossen, D.L.; Imhof, A.; van Blaaderen, A. General Method to Coat Colloidal Particles with Silica. *Langmuir* **2003**, *19*, 6693–6700. [CrossRef]
24. Palacios, L.R.G.; Martinez, S.M.; Tettamanti, C.S.; Inda, A.; Quinteros, D.A.; Bracamonte, A.G. Bi-coloured Enhanced Luminescence Imaging by targeted switch on/off Laser MEF coupling for synthetic Biosensing of Nanostructured Human Serum Albumin. *Photochem. Photobiol. Sci.* **2023**, *22*, 2735–2758. [CrossRef]
25. Hermanson, G.T. *Bioconjugate Techniques*, 2nd ed.; Elsevier: Amsterdam, The Netherlands, 2008.
26. Trotta, F.; Martina, K.; Robaldo, B.; Barge, A.; Cravotto, G. Recent advances in the synthesis of cyclodextrin derivatives under microwaves and power ultrasound. *J. Incl. Phenom. Macrocycl. Chem.* **2007**, *57*, 3–7. [CrossRef]
27. Brady, B.; Lynam, N.; O'Sullivan, T.; Ahern, C.; Darcy, R. 6-O-ptoluenesulfonyl-cyclodextrin. *Org. Synth.* **2004**, *77*, 220–236.
28. Gascon, J.M.; Oliveri, V.; McGown, A.; Kaya, E.; Chen, Y.L.; Austin, C.; Walker, M.; Platt, F.M.; Vecchio, G.; Spencer, J. Synthesis and Study of Multifunctional Cyclodextrin–Deferasirox Hybrids. *ChemMedChem* **2019**, *14*, 1484–1492. [CrossRef]
29. Paramelle, D.; Sadovoy, A.; Gorelik, S.; Free, P.; Hobley, J.; Fernig, D.G. A rapid method to estimate the concentration of citrate capped silver nanoparticles from UV-visible light spectra. *Analyst* **2014**, *139*, 4855–4861. [CrossRef]
30. Enustun, B.V.; Turkevich, J. Coagulation of Colloidal gold. *J. Am. Chem. Soc.* **1963**, *85*, 3317–3328. [CrossRef]
31. Schulz, F.; Homolka, T.; Bastús, N.G.; Puntes, V.; Weller, H.; Vossmeyer, T. Little Adjustments Significantly Improve the Turkevich Synthesis of Gold Nanoparticles. *Langmuir* **2014**, *30*, 10779–10784. [CrossRef]
32. Bracamonte, A.G.; Brouard, D.; Lessard-Viger, M.; Boudreau, D.; Veglia, A.V. Nano-supramolecular complex synthesis: Switch on/off enhanced fluorescence control and molecular release using a simple chemistry reaction. *Microchem. J.* **2016**, *128*, 297–304. [CrossRef]
33. In den Kirschen, O.W.; Hutchinson, W.; Bracamonte, A.G. Conjugation Reactions of Hybrid Organosilanes for Na-noparticles and surface modifications. *J. Chem. Res. Adv.* **2021**, *2*, 6–15.

34. Ishibe, T.; Maeda, Y.; Terada, T.; Naruse, N.; Mera, Y.; Kobayashi, E.; Nakamura, Y. Resistive switching memory performances in oxide hetero-nanocrystals with well-controlled interfaces. *Sci. Technol. Adv. Mater.* **2020**, *21*, 195–204. [CrossRef] [PubMed]
35. Tian, G.; Zhang, F.; Yao, J.; Fan, H.; Li, P.; Li, Z.; Song, X.; Zhang, X.; Qin, M.; Zeng, M.; et al. Magnetoelectric Coupling in Well-Ordered Epitaxial BiFeO3/CoFe2O4/SrRuO3 Heterostructured Nanodot Array. *ACS Nano* **2016**, *10*, 1025–1032. [CrossRef] [PubMed]
36. Palacios, L.R.G.; Veglia, A.; Bracamonte, A.G. Inflow nano-optics from the near-to the far-field detection based on Metal-Enhanced Fluorescence signaling. *Microchem. J.* **2021**, *169*, 106539. [CrossRef]
37. Brouard, D.; Viger, M.L.; Bracamonte, A.G.; Boudreau, D. Label-free biosensing based on multilayer fluorescent nanocomposites and a cationic polymeric transduce. *ACS Nano* **2011**, *5*, 1888–1896. [CrossRef]
38. Strobbia, P.; Languirand, E.R.; Cullum, B.M. Recent advances in plasmonic nanostructures for sensing: A review. *Opt. Eng.* **2015**, *54*, 100902. [CrossRef]
39. Su, K.-H.; Wei, Q.-H.; Zhang, X.; Mock, J.J.; Smith, D.R.; Schultz, S. Interparticle Coupling Effects on Plasmon Resonances of Nanogold Particles. *Nano Lett.* **2003**, *3*, 1087–1090. [CrossRef]
40. Xia, B.; He, F.; Li, L. Metal-enhanced fluorescence using aggregated silver nanoparticles, Colloids and Surfaces A: Physicochem. *Eng. Asp.* **2014**, *444*, 9–14. [CrossRef]
41. Saravanan, S.; Dubey, R. Synthesis of SiO_2Nanoparticles by Sol-Gel Method and Their Optical and Structural Properties, Rom. *J. Inf. Sci. Technol.* **2020**, *23*, 105–112.
42. Kandori, H. Structure/function study of photoreceptive proteins by FTIR spectroscopy. *Bull. Chem. Soc. Jpn.* **2020**, *93*, 904–926. [CrossRef]
43. Conde, J.; Rosa, J.; Lima, L.C.; Baptista, P.V. Nanophotonics forMolecular Diagnostics and Therapy Applications. *Int. J. Photoenergy* **2012**, *2012*, 619530. [CrossRef]
44. Abbe, E. Archiv Microskop. *Anatomy* **1873**, *9*, 413.
45. Axelrod, D. Selective imaging of surface fluorescence with very high aperture microscope objectives. *J. Biomed. Opt.* **2001**, *6*, 6–13. [CrossRef] [PubMed]
46. Luchowski, R.; Calander, N.; Shtoyko, T.; Apicella, E.; Borejdo, J.; Gryczynski, Z.K.; Gryczynski, I. Plasmonic platforms of self-assembled silver nanostructures in application to fluorescence. *J. Nanophotonics* **2010**, *4*, 043516. [CrossRef] [PubMed]
47. Boudreau, D.; Bracamonte, A.G. Bitacora Digital. 2019. Available online: https://revistas.unc.edu.ar/index.php/Bitacora/issue/view/2180/394 (accessed on 8 March 2024).
48. Gontero, D.; Veglia, A.V.; Boudreau, D.; Bracamonte, A.G. Ultraluminescent gold Core@shell nanoparticles applied to individual bacterial detection based on Metal-Enhanced Fluorescence Nanoimaging. *J. Nanophotonics* **2017**, *12*, 012505. [CrossRef]
49. Veglia, A.V.; Bracamonte, A.G. Metal Enhanced fluorescence emission and Quenching protection effect with a host-guest Nanophotonic-supramolecular structure. *J. Nanophotonics* **2018**, *12*, 033004. [CrossRef]
50. Darvill, D.; Centeno, A.; Xie, F. Plasmonic fluorescence enhancement by metal nanostructures: Shaping the future of bionanotechnology. *Phys. Chem. Chem. Phys.* **2013**, *15*, 15709–15726. [CrossRef] [PubMed]
51. Gontero, D.; Lessard-Viger, M.; Brouard, D.; Bracamonte, A.G.; Boudreau, D.; Veglia, A.V. Smart Multifunctional Nanoparticles design as Sensors and Drug delivery systems based on Supramolecular chemistry. *Microchem. J.* **2017**, *130*, 316–328. [CrossRef]
52. Giljohann, D.A.; Seferos, D.S.; Daniel, W.L.; Massich, M.; Patel, P.C.; Mirkin, C.A. Gold Nanoparticles for Biology and Medicine. *Angew. Chem. Int. Ed.* **2010**, *49*, 3280–3294. [CrossRef]
53. Liu, C.; Capjack, C. Effects of cellular fine structure on scattered light pattern. *IEEE Trans. NanoBiosci.* **2006**, *5*, 76–82. [CrossRef]
54. Lin, P.; Owens, R.; Tricot, G.; Wilson, C.S. Flow Cytometric Immunophenotypic Analysis of 306 Cases of Multiple Myeloma. *Am. J. Clin. Pathol.* **2004**, *121*, 482–488. [CrossRef]
55. Charitidis, C.A.; Georgiou, P.; Koklioti, M.A.; Trompeta, A.-F.; Markakis, V. Manufacturing nanomaterials: From research to industry. *Manuf. Rev.* **2014**, *1*, 11. [CrossRef]
56. Wang, Y.; Li, P.; Tran, T.T.-D.; Zhang, J.; Kong, L. Manufacturing Techniques and Surface Engineering of Polymer Based Nanoparticles for Targeted Drug Delivery to Cancer. *Nanomaterials* **2016**, *6*, 26. [CrossRef] [PubMed]
57. Bracamonte, A.G. Design of new High Energy near Field Nanophotonic materials for far Field applications. In *Advances in Nanocomposite Materials for Environ-Mental and Energy Harvesting Applications*; Part of the Springer Book Series: Engineering Materials; Springer Nature: Cham, Switzerland, 2022; Chapter 28; pp. 859–920, ISBN 9783030943189. [CrossRef]